Investigating the Global OH Radical Distribution Using Steady-State Approximations and Satellite Data

Matilda A. Pimlott[1], Richard J. Pope[1,2], Brian J. Kerridge[3,4], Barry G. Latter[3,4], Diane S. Knappett[3,4], Dwayne E. Heard[5], Lucy J. Ventress[3,4], Richard Siddans[3,4], Wuhu Feng[1,6], Martyn P. Chipperfield[1,2]

[1]School of Earth and Environment, University of Leeds, Leeds, LS2 9JT, UK
[2]National Centre for Earth Observation, University of Leeds, Leeds, LS2 9JT, UK
[3]Remote Sensing Group, STFC Rutherford Appleton Laboratory, Chilton, Oxfordshire, OX11 0QX, UK
[4]National Centre for Earth Observation, STFC Rutherford Appleton Laboratory, Chilton, Oxfordshire, OX11 0QX, UK
[5]School of Chemistry, University of Leeds, Leeds, LS2 9JT, UK
[6]National Centre for Atmospheric Science, University of Leeds, Leeds, LS2 9PH, UK

Correspondence to: Matilda A. Pimlott (eemap@leeds.ac.uk)

Abstract. We present a novel approach to derive indirect global information on the hydroxyl radical (OH), one of the most important atmospheric oxidants, using state-of-art satellite trace gas observations (key sinks and sources of OH) and a steady-state approximation (SSA). This is a timely study as OH observations are predominantly from spatially sparse field and infrequent aircraft campaigns, so there is a requirement for further approaches to infer spatial and temporal information on OH and its interactions with important climate (e.g. methane, CH_4) and air quality (e.g. nitrogen dioxide, NO_2) trace gases. Due to the short lifetime of OH (~1 s), SSAs of varying complexities can be used to model its concentration and offer a tool to examine the OH budget in different regions of the atmosphere. Here, we use the well-evaluated TOMCAT three-dimensional chemistry transport model to identify atmospheric regions where different complexities of the SSAs are representative of OH. In the case of a simplified SSA (S-SSA), where we have observations of ozone (O_3), carbon monoxide (CO), CH_4 and water vapour (H_2O) from the Infrared Atmospheric Sounding Interferometer (IASI) on-board ESA's MetOp-A satellite, it is most representative of OH between 600 and 700 hPa (though suitable between 400–800 hPa) within ~20–30 % of TOMCAT modelled OH. The same S-SSA is applied to aircraft measurements from the Atmospheric Tomography Mission (ATom) and compares well with the observed OH concentrations within ~26 % yielding a correlation of 0.78. We apply the S-SSA to IASI data spanning 2008–2017 to explore the global long-term inter-annual variability of OH. Relative to the 10-year mean, we find that global annual mean OH anomalies ranged from -3.1 % to +4.7 %, with the largest spread in the tropics between -6.9 % and +7.7 %. Investigation of the individual terms in the S-SSA over this time period suggests that O_3 and CO were the key drivers of variability in the production and loss of OH. For example, large enhancement in the OH sink during the positive 2015/2016 ENSO event was due to large scale CO emissions from drought induced wildfires in South East Asia. The methodology described here could be further developed as a constraint on the tropospheric OH distribution as additional satellite data becomes available in the future.

Introduction

The hydroxyl radical (OH) is a key species in atmospheric chemistry as it largely determines the oxidation capacity of the troposphere, and therefore the lifetimes of many different species. Key species controlled by OH include important greenhouse gases (e.g. methane, CH_4), ozone-depleting substances (e.g. hydrochlorofluorocarbons), as well as other short-lived anthropogenic and natural pollutants (e.g. volatile organic compounds (VOCs), nitrogen oxides (NO_x) and carbon monoxide (CO)) (Lelieveld et al., 2016). The importance of OH to tropospheric oxidation capacity was recognised in the early 1970s (Levy, 1971) and has been subject to many scientific investigations since, especially in relation to the lifetime of CH_4 e.g. McNorton et al. (2016), Rigby et al. (2017) and Turner et al. (2019). A better understanding of the spatial and temporal distribution of OH, the primary sink of CH_4, would aid the interpretation of recent trends in CH_4, such as the 2000–2007 concentration stabilisation period (Turner et al., 2019).

The primary source of OH in the remote troposphere is the photolysis of ozone (O_3) by ultraviolet (UV) radiation (< 330 nm wavelength). This forms $O(^1D)$ which then reacts with water vapour (H_2O) to form OH (Lelieveld et al., 2016):

$$O_3 + hv \ (\lambda < 330 \ nm) \rightarrow O(^1D) + O_2 \tag{1}$$

$$O(^1D) + H_2O \rightarrow 2OH \tag{2}$$
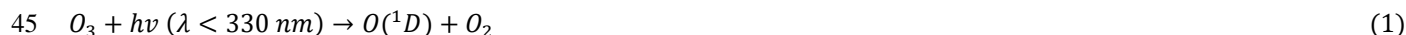
The OH radical formed is very reactive due to the unpaired electron on the oxygen atom. After formation, the OH radicals attack reduced and partly oxidised gases, removing them from the atmosphere and forming peroxy radicals (e.g. hydroperoxyl radical, HO_2). The peroxy radicals can go on to form peroxides and participate in many other atmospheric chemistry reactions (e.g. ozone formation) and can also go on to reform OH (Lelieveld et al., 2016).

Direct in situ measurements of OH are scarce as the measurement process is challenging with few instruments available (Stone et al., 2012; Lelieveld et al., 2016). Due to its very short lifetime, ~1 second in the daytime, the abundance of OH is very low with the global tropospheric mean OH concentration is around 1×10^6 molecule cm^{-3} ~~Direct in situ measurements of OH are scarce due to its very short lifetime, ~1 second in the daytime, and low abundance; the global tropospheric mean OH concentration is around 1×10^6 molecule cm^{-3} (Lelieveld et al., 2016; Stone et al., 2012)~~. In situ OH measurements are limited to field campaigns at specific locations (Stone et al., 2012) and aircraft missions e.g. NASA's Atmospheric Tomography mission (ATom) (Wofsy et al., 2018; Brune et al., 2020). There has consequently been a demand for indirect methods to infer global-scale OH. An established method is to use the methyl chloroform (CH_3CCl_3, MCF) concentrations to derive a global mean OH concentration by using inverse modelling which exploits the fact that sources of MCF are well known and that its main sink is reaction with OH (Lovelock, 1977; Singh, 1977; Prinn et al., 1992). This method has been used to study the temporal variability of OH (Montzka et al., 2011; Prinn et al., 2005). The accuracy of this method depends on accurate estimates of MCF emissions. MCF production is regulated under the legislation initiated by the 1987 Montreal Protocol and therefore MCF has seen a sharp decline in atmospheric abundance since the mid-1990s, which will reduce the

65   viability of this method, leading to new methods and tracers being sought (Huang and Prinn, 2002; Liang et al., 2017; Rigby et al., 2017).

However, the above-mentioned MCF method is unable to provide spatial information on OH. In the last two decades, there has been an increasing wealth of tropospheric satellite data, providing information on the spatial and temporal variability of

70   atmospheric species, but not OH (Streets et al., 2013). These atmospheric composition data are global in extent and now span more than a decade, so have the potential to provide information to infer a global OH distribution and its variation over time. Presently, there are limited examples of the use of satellite data to infer global OH. In a recent study, Wolfe et al. (2019) used satellite formaldehyde observations and budget to calculate remote tropospheric column OH, developing the method using aircraft data from ATom to establish formaldehyde production/loss and OH concentrations.

75

To exploit satellite data here, we use a simplified steady-state approximation. This is an appropriate assumption due to the very short daytime lifetime of OH and the simplification is described in Sect. 2 below. Some studies have thus far used steady-state approximations to calculate OH from in situ surface data at field sites e.g. Eisele (1996) at Mauna Loa Observatory, Savage et al. (2001) and Smith et al. (2006) at the Mace Head Atmospheric Research Centre, Ireland, Creasey

80   et al. (2003) at Cape Grim in the Southern Ocean, and Slater et al. (2020) in central Beijing. However, there is also the potential for these approximations to be applied to satellite data in a global context. The use of the steady-state approximations has had varied success. Eisele (1996) found that the comparison between observed and calculated OH depended on which air mass was present, with free tropospheric air masses showing better agreement than air masses from the boundary layer. Savage et al. (2001) found a good correlation between measured and calculated OH, but a steady-state

85   overprediction of around 30 %. Models using only simplified chemistry have been shown to capture the chemistry of unpolluted regions. Sommariva et al. (2004) used a 'detailed' and 'simple' box-model to study OH in unpolluted marine air at Cape Grim in the Southern Hemisphere (SH). The 'simple' box-model, based only on CO, CH_4 and inorganic reactions, agreed within 5–10 % of the 'detailed' box-model that also contained non-methane hydrocarbons (NMHCs). The models over-estimated the measured OH by 10–20 %.

90

OH reactivity (OHR), the inverse of OH lifetime, is also measured in the field to provide additional information on the tropospheric oxidation capacity and abundance of the OH radical. OHR can be measured in situ along with trace gas concentrations e.g. during aircraft campaigns such as NASA's ATom (Wofsy et al., 2018). Observed OHR is commonly compared to calculated OHR by summing individual sink terms using measured reactant concentrations multiplied by their

95   respective reaction rate co-efficients with OH (Yang et al., 2016). However, a large number of field campaigns have shown that there is often a substantial difference between observed in situ and calculated OHR, known as the "missing" reactivity (Ferracci et al., 2018). This "missing" reactivity can account for as much as 20 % (usually outside the OHR uncertainty range) to 80 % of the observed OHR (Yang et al., 2016). There are many proposed reasons for this "missing" reactivity, such

as short-lived VOCs that were not measured (Kovacs et al., 2003) or in the rainforests some mixture of unidentified biogenic emissions and photo-oxidation products (Edwards et al., 2013; Nölscher et al., 2016).

An improved characterisation of the OH temporal variation is vital to understanding key aspects of atmospheric chemistry, such as interannual to decadal variability in methane (Turner et al., 2019; Zhao et al., 2020). Studies using MCF observations, in combination with box-model analyses, show similar annual OH anomalies between 1995 and 2010, with a broadly negative anomaly of -6 to 0 % between 1995 and 1999, a positive anomaly of 0 to 6 % between 1999 and 2007 and a negative anomaly of -5 to 0 % between 2007 and 2010 (Montzka et al., 2011; Rigby et al., 2017; Turner et al., 2017; Patra et al., 2021). After 2010, the results of such studies differ with some showing consistently negative anomalies of -4 to 0 % between 2010 and 2018 (Rigby et al., 2017; Turner et al., 2017) and others showing some positive anomalies in this period, for example in the range of 0 to 4 % between 2010 and 2015 (Naus et al., 2019; Patra et al., 2021). Studies using chemical transport models are not consistent with those using MCF observations. He et al., (2020) found negative anomalies of -5 to 0 % between 1995 and 2005 and then positive anomalies of 0 to 4 % between 2005 and 2017. A study by Zhao et al., (2020) found a multi-model mean increase of 0.7×10^5 molecule cm^{-3} between 1980 and 2010, equivalent to around 0.1–0.5 % yr^{-1}, with the greatest rate of increase in the final decade (2000–2010). The OH increase from 2000–2010 was predominantly due to that in the primary production term ($O(^1D) + H_2O$) though also to a decrease in the CO sink term ($OH + CO$). Model studies further show OH interannual variability to be influenced by the El Niño-Southern Oscillation (ENSO), with low OH concentrations being associated with El Niño years and high OH concentrations with La Niña years (Zhao et al., 2020; Anderson et al., 2021).

Here, we use output data from the TOMCAT 3-D chemical transport model to explore the validity of OH steady-state approximations in the troposphere. A simplified steady-state approximation is then applied to observations of O_3, CO, CH_4 and H_2O mid-tropospheric concentrations retrieved from observations by the Infrared Atmospheric Sounding Interferometer (IASI) instrument on-board the MetOp-A satellite in 2010 and 2017. This calculated satellite OH is then compared to OH from TOMCAT using full chemistry and ATom observations. Finally, the simplified approximation is applied to MetOp-A data over a 10-year period (2008–2017) to infer the temporal variability in OH. Section 2 describes how steady-state approximations, TOMCAT model, aircraft and satellite data are employed in this study. Section 3 presents the results and discussion. Section 4 summarises our conclusions.

2 Methods

2.1 OH steady-state approximations

Due to the short lifetime of OH, a steady-state approximation can be used to model its concentration. The approximation can be defined as Eq. (3):

$$[OH]_{Steady\ State} = \frac{k_{A+B}[A][B]+\ldots+j_C[C]+\ldots}{\sum k_D[D]+\ldots} \tag{3}$$

where the numerator of the expression represents a sum of the source terms. k_{A+B} is the reaction rate constant of A and B to form OH and j_C is the photolysis co-efficient of C to form OH. The denominator represents a sum of the sink terms. k_D is the reaction rate constant of D and OH, where D represents an individual sink species. The accuracy of the approximation depends partly on the number of source and sink terms which can be included. This, in turn, depends on the availability of observations to provide a constraint for each of those terms.

Here, we use three steady-state approximations of different complexity, summarised in Supplementary Table S1. The most complex is referred to as the full chemistry steady-state approximation (FC-SSA) and contains the largest number of source and sink terms, capturing the most comprehensive tropospheric chemistry, with 26 source terms and 51 sink terms. The second most complex is based on a steady-state approximation in Savage et al. (2001) (Sav-SSA) and contains 5 source and 12 sink terms. Lastly, we propose a simplified steady-state approximation (S-SSA) containing 1 source term (based on Eq. (1) and Eq. (2)) and 3 sink terms (based on the reaction of OH with CH_4, CO and O_3). The S-SSA allows OH to be derived using only the main tropospheric source and sinks, that can be directly observed by satellite. We adopt the S-SSA as Eq. (4):

$$[OH]_{Steady\ State}$$

$$= \frac{\frac{2j_1k_1[O_3][H_2O]}{k_2[N_2] + k_3[O_2]}\left(\frac{2j_1k_1[O_3][H_2O]}{k_2[N_2] + k_3[O_2] + k_1[H_2O]}\right)}{k_4[CH_4] + k_5[CO] + k_6[O_3](k_4[CH_4] + k_5[CO] + k_6[O_3])}$$

where j_1 is the photolysis co-efficient for $O_3 \rightarrow O(^1D) + O_2$, k_1 is the reaction rate constant for $O(^1D) + H_2O$, k_2 and k_3 are the collisional relaxation rate constants with respect to N_2 and O_2, k_4, k_5 and k_6 are the rate constants for reaction of OH with CH_4, CO and O_3, respectively. The expression implicitly assumes a steady state for the production and loss of $O(^1D)$.

2.2 OH reactivity

OHR, the denominator of Eq. (3), can be directly observed or calculated using a model and/or observed species. The accuracy of an OHR calculation is similarly dependent on the number of sink terms which can be included and the availability of requisite observations. In principle, examination of OHR measurements co-located with those of [OH] could allow steady-state approximations for OH sources and sinks to be evaluated separately. We adopt the denominator of Eq. (4) as a simplified expression for OHR as Eq. (5):

$$[OHR] = k_4[CH_4] + k_5[CO] + k_6[O_3] \tag{5}$$

2.3 Model and observations

2.3.1 TOMCAT 3-D model

In this study we use the 3-D global chemical transport model TOMCAT (Chipperfield, 2006) at a $2.8° \times 2.8°$ resolution with
160 31 vertical levels between the surface and 10 hPa. The model is coupled with the Global Model of Aerosol Processes (GLOMAP) to calculate aerosol microphysics (Mann et al., 2010). The model is forced by meteorological reanalyses (ERA-Interim) from the European Centre for Medium-Range Weather Forecasts (ECMWF) (Dee et al., 2011). The tropospheric chemistry scheme is described in Monks et al. (2017), with the main updates as follows: Anthropogenic and natural surface emissions from the Coupled Model Intercomparison Project Phase 6 (CMIP6) for NO_x, CO and VOCs (Feng et al., 2020);
165 fixed annual biogenic emissions from the Chemistry-Climate Model Initiative (CCMI) (Morgenstern et al., 2017); biomass burning emissions from the Global Fire Emissions Database (GFED) version 4 (van der Werf et al., 2017); CH_4 scaled to a best estimate based on the 2010 globally averaged surface CH_4 value from NOAA (Dlugokencky, 2020) and an update to the cloud fields using reanlyses from ECMWF (as described in Rowlinson et al. (2019)). The model simulation was run for 2010 and 2017, with 6 months of spin up in each case. The simulation was sampled daily at 9:30 am local time globally to match
170 the MetOp-A daytime overpass time.

Monks et al. (2017) and Rowlinson et al. (2019) have evaluated TOMCAT OH compared to model and observational datasets for the year 2000. The set-up for the simulations used in Rowlinson et al. (2019) is most similar to that in this study, but broadly the simulation in Monks et al. (2017) produces similar regional zonal OH values. TOMCAT OH in Rowlinson et
175 al. (2019) had an average global tropospheric concentration of 1.04×10^6 molecule cm^{-3}, which sits within a range from other studies e.g. $0.94 \pm 0.1 \times 10^6$ molecule cm^{-3} from inferred OH observations from MCF by Prinn et al. (2001), $1.08 \pm 0.6 \times 10^6$ molecule cm^{-3} from the POLARCAT Model Intercomparison Project (POLMIP) and the multi-model mean of 1.11 ± 0.2 $\times 10^6$ molecule cm^{-3} from 16 Atmospheric Chemistry and Climate Model Intercomparison Project (ACCMIP) models (Naik et al., 2013). In terms of vertical distribution, Monks et al. (2017) and Rowlinson et al. (2019) show the maximum TOMCAT
180 OH values to be between the surface and 750 hPa near the equator. In comparison, Spivakovsky et al. (2000) (MCF method) and the multi-model mean OH from ACCMIP (Naik et al., 2013) have peak OH values higher up in the troposphere. Overall, in the mid-troposphere, the primary focus in this study, Rowlinson et al. (2019) TOMCAT OH shows comparable values across all the latitude regions in comparison with Spivakovsky et al. (2000) and ACCMIP (Naik et al., 2013).

185 Monks et al. (2017) investigated TOMCAT CO, O_3 and OH and showed that the model is able to capture the main seasonal and spatial features of CO and O_3. TOMCAT has a slightly higher global mean tropospheric OH concentration (1.08×10^6 molecule cm^{-3}) than inferred OH observations from MCF e.g. $0.94 \pm 0.1 \times 10^6$ molecule cm^{-3} by Prinn et al. (2001). TOMCAT has a similar or lower global mean tropospheric OH concentration than multi-model values from several intercomparison studies e.g. $1.08 \pm 0.6 \times 10^6$ molecule cm^{-3} from the POLARCAT Model Intercomparison Project (POLMIP)

2.3.2 Satellite observations

195   We use satellite observations for 2010 and 2017 from the MetOp-A satellite launched by EUMETSAT in 2006. MetOp-A is in a polar sun-synchronous orbit which crosses the equator at ~9:30 (day overpass) and 21:30 (night overpass) giving global earth coverage twice a day (Clerbaux et al., 2009). Here, we use height-resolved distributions of CO, CH_4, O_3 and H_2O retrieved from MetOp-A observations by schemes developed by the Rutherford Appleton Laboratory (RAL). The O_3, CO and H_2O retrievals are from the extended version of RAL's Infrared and Microwave Sounding (IMS-extended) scheme,

200   which co-retrieves temperature profiles, cloud and surface properties, other trace gases and aerosols and is documented in the supplement of Pope et al. (2021). The CH_4 data were produced by an improved version (v2.0) of RAL's methane retrieval scheme (Siddans et al., 2020) developed for IASI on MetOp-A. The original IASI methane scheme (v1.0) was described in Siddans et al. (2017). For the IMS-extended scheme, as well as the IASI methane scheme, retrieved profiles are output at the locations of IASI soundings. IASI is a nadir-viewing thermal infrared Fourier Transform Spectrometer, with a spectral range

205   from 645 to 2760 cm^{-1} (Clerbaux et al., 2009). It samples a swath width of 2200 km by scanning a set of four fields of view across-track. At nadir, these are circular with 12 km diameter, occupying a square 50 km × 50 km (3.3° × 3.3°). For the study of OH temporal variation between 2008 and 2017, MetOp-A data sub-sampled both temporally (1 in 10 days) and spatially (1 in 4 pixels) were available. Supplementary Figs. S1 and S2 show good agreement between the sub-sampled and fully sampled satellite data in a zonal average when compared in 2010 and 2017, with an average monthly correlation coefficient

210   in latitudinal structure of 0.89 and 0.85, respectively.

Profiles of H_2O, O_3 and CO, along with temperature, are represented on a set of 101 levels in the IMS extended scheme. For H_2O, information from IASI and the two microwave sounders (Microwave Humidity Sounder (MHS) and Advanced Microwave Sounding Unit (AMSU-A)) is sufficient to resolve a number of independent layers between the surface and 200

215   hPa, with degrees of freedom of signal (DOFS) being typically ~10. Profiles of H_2O (and temperature) produced from Metop-A by the IMS core scheme have been validated against radiosondes in ESA's Climate Change Initiative (European Space Agency, n.d.) and found to have a systematic bias of ~10%. For CO, on the other hand, measurement information (exclusively from IASI) is sufficient to retrieve only one independent layer with the averaging kernels centred on the mid troposphere ~600 hPa with a full width half medium (FWHM) from ~300–900 hPa, as seen in Figs. S3 and S4. Validation of

220   the IMS-extended CO retrievals, through indirect comparisons using the Copernicus Atmospheric Monitoring Service (CAMS) in which averaging kernels were applied (see the supplement of Pope et al. (2021)), found uncertainty in retrieved CO to be approximately 10%. For O_3, averaging kernels peak at a number of levels spanning the troposphere and

stratosphere with DOFs generally ranging between 3.0 and 4.0. The lowest peak is seen in Figs. S3 and S4 to be around ~600 hPa with FWHM from ~350–900h Pa. When compared with ozonesondes (Supplementary Sect. S3), O_3 retrieved in the mid-troposphere by the IMS-extended scheme is found to be differ systematically larger by up to 20 %. The RAL v2.0 IASI scheme retrieves CH_4 on a set of coarsely spaced levels, taking as input temperature profiles and surface spectral emissivity pre-retrieved from the same soundings by IMS. Output files also include layer-average mixing ratios and their corresponding averaging kernels, as shown in Figs. S3 and S4. The number of DOFS is greater than 2 in the tropics and drops to below 2 at polar latitudes; the surface–450 hPa layer average is well resolved from layers above. Examples of averaging kernels for H_2O, CH_4, CO and O_3 are shown in Supplementary Sect. S2 (Figs. S3 and S4).

With the exception of H_2O, retrieval sensitivity is seen in Figs. S3 and S4 to decrease in the lowest atmosphere as temperature approaches that of the surface and surface-air temperature contrast on which sensitivity depends diminishes. However, in all four cases, averaging kernels for layers centred in the mid-troposphere are well behaved, with peaks around 600–700 hPa and FWHMs contained within the free troposphere, as appropriate for the focus of this study. For straightforward comparison with TOMCAT simulations, use of retrieved MetOp-A data is further restricted to the 400–800 hPa and 600–700 hPa layers, where averaging kernels peak, rather than applying the averaging kernels to model profiles.

Co-located retrievals of H_2O, O_3 and CO data and CH_4 were filtered for a geometric cloud fraction of 20 % or less (i.e. 0.2 fractional coverage or less). This resulted in satellite soundings which exclude all opaque clouds which fill the field of view and a fraction of clouds which fill part of the field of view. In comparison with TOMCAT, which had no filtering for cloud, this could produce a clear skies bias. However, the model is driven by ECMWF meteorological fields, which are also used in the satellite retrieval, so they should be reasonably consistent. Figure S6 shows the daily average number of retrievals used per grid box for the calculation of satellite [OH]. Globally, the daily average number of grid-box profile retrievals for the input species ranges between 0 and 24, with an average of ~6. Therefore, there are sufficient retrievals of the trace gases in the S-SSA to calculate values of OH for most grid-boxes every day.

Uncertainty on [OH] calculated with the S-SSA using satellite data is estimated from the systematic errors on the four retrieved species, as described in Supplementary Sect. S6, to be ~23–24 % (Fig. S7). This assumes that there is no uncertainty in the rate constants (j_1, k_{1-6}), which is a potential source of error.

2.3.3 ATom observations

The ATom mission observed many atmospheric variables, including OH and OHR (Wofsy et al., 2018). NASA's DC-8 aircraft sampled the atmosphere between 0.2–12 km altitude during four campaigns between 2016–2018, sampling both hemispheres over the Pacific and Atlantic Oceans. We use ATom observations of OH, OHR, O_3, CO, CH_4, H_2O and j_1. We

use data from all four campaigns between and 08:00–11:00 local solar time, to compare with the 09:30 MetOp-A overpass time and the 600–700 hPa pressure range, where the S-SSA agrees best with the full chemistry (see Sect. 3.1). The data are also filtered to remove measurements influenced by stratospheric air (O_3/CO > 1.25) or biomass burning (acetonitrile concentration > 200 ppt), as in Travis et al. (2020). The OH and OHR observations used in this study were made by the ATHOS instrument (Faloona et al., 2004; Brune et al., 2020). Wofsy et al. (2018) merged the observations into a two minute sampling interval. The uncertainty on the OH observations from the ATHOS instrument at the 2σ confidence level is ± 35 % and the limit of detection of the OH observations is 0.018 pptv. The uncertainty on the OHR observations from the ATHOS instrument at the 2σ confidence level is ± 0.8 s^{-1}. The NOAA Picarro instrument provides CH_4 and CO observations, with uncertainties of ± 0.7 ppbv and ± 8.9 ppbv, respectively (Karion et al., 2013). The Diode laser hygrometer (DLH) provides H_2O observations with an uncertainty of ± 5 % (Podolske et al., 2003). The NOAA-NO$_y$ O_3 instrument provides O_3 observations with an average uncertainty of ± 2.0 ppb (Ryerson et al., 2000). The CCD Actinic Flux Spectroradiometers (CAFS) instrument provides j_1 observations, with an uncertainty of ± 20 % (Shetter and Müller, 1999).

3 Results & Discussion

3.1 Application of the simplified steady-state approximation

3.1.1 Application to model data

We use the TOMCAT output of CO, CH_4, O_3 and H_2O, for 2010 in the S-SSA of OH to determine the validity of this approximation in different regions of the troposphere. Mass-weighted zonal mean [OH] calculated with the S-SSA and modelled TOMCAT [OH] are compared in Fig.1. Table 1 shows the differences to be very large (>85 %) between global mean TOMCAT OH and TOMCAT S-SSA OH at pressures <400 hPa (i.e. upper troposphere and stratosphere). Nearer the surface (>800 hPa) the S-SSA shows a good zonal mean agreement (< 6 % difference). However, there are large differences in the longitude-latitude distribution which do not show in the zonal mean and we do not expect a good approximation of the complex OH chemistry in the boundary layer using our simplified approximation. Therefore, we focus our investigation at pressure levels above the boundary layer.

The mid tropospheric region (400–800 hPa) shows good agreement in spatial distribution and abundance with a S-SSA global mean underestimate of ~30–35 %. In the mid-troposphere, there are peak values of 5.4 ×10^6 molecule cm^{-3} (Jan) and 7.3 ×10^6 molecule cm^{-3} (Jun) for TOMCAT S-SSA OH, which are comparable to peak values of 5.6 ×10^6 molecule cm^{-3} (Jan) and 8.3 ×10^6 molecule cm^{-3} (Jun) for TOMCAT OH. Within this mid-tropospheric region, the 600–700 hPa layer is further investigated, as it shows better agreement in the zonal mean structure and global mean than the larger pressure region, as shown in Table 1. TOMCAT output from 2017 was also applied to the S-SSA with similar results, shown in Supplementary Sect. S7 (Fig. S9). We therefore selected the pressure region 600–700 hPa for investigation because of the

good agreement between TOMCAT OH and TOMCAT S-SSA OH in this region. OH in this the pressure region contributes to ~15 % of the tropospheric OH burden. Diagnosis of the model output shows the influence of OH in this region to methane oxidation is slightly larger, with a contribution of ~19 % of methane-loss-weighted OH.

290

Figure 2 shows the spatial differences between the TOMCAT and S-SSA OH. In January, the S-SSA shows an underestimate of up to ~2 $\times 10^6$ molecule cm^{-3} across the Northern Hemisphere (NH) and over parts of the oceans across the SH, mostly between the equator and 30°S e.g. the Atlantic, edges of the Pacific, but not the Indian Ocean. In the SH, an overestimate is present over some of the continents, e.g. up to ~2 $\times 10^6$ molecule cm^{-3} in S America, and up to ~1 $\times 10^6$

295   molecule cm^{-3} in the Indian Ocean and the centre of the Pacific. Broadly, the peak [OH] values across SE Indian Ocean and S African continent show good agreement. In June, the S-SSA shows good agreement over the oceans in the NH, mostly between the equator and 30°N, and the S American and Australian continent in the SH. An overestimate of up to ~4 $\times 10^6$ is found across the peak [OH] values found across the N African continent and China. A slight underestimate of up to ~1 $\times 10^6$ is found on landmasses around the equator.

300

In summary, the S-SSA agrees with TOMCAT across the oceans near the equator, to an extent which depends on the season. The peak values of [OH] are found in similar locations for TOMCAT and S-SSA [OH], however, the S-SSA generally produces an underestimate of these peak values.

305
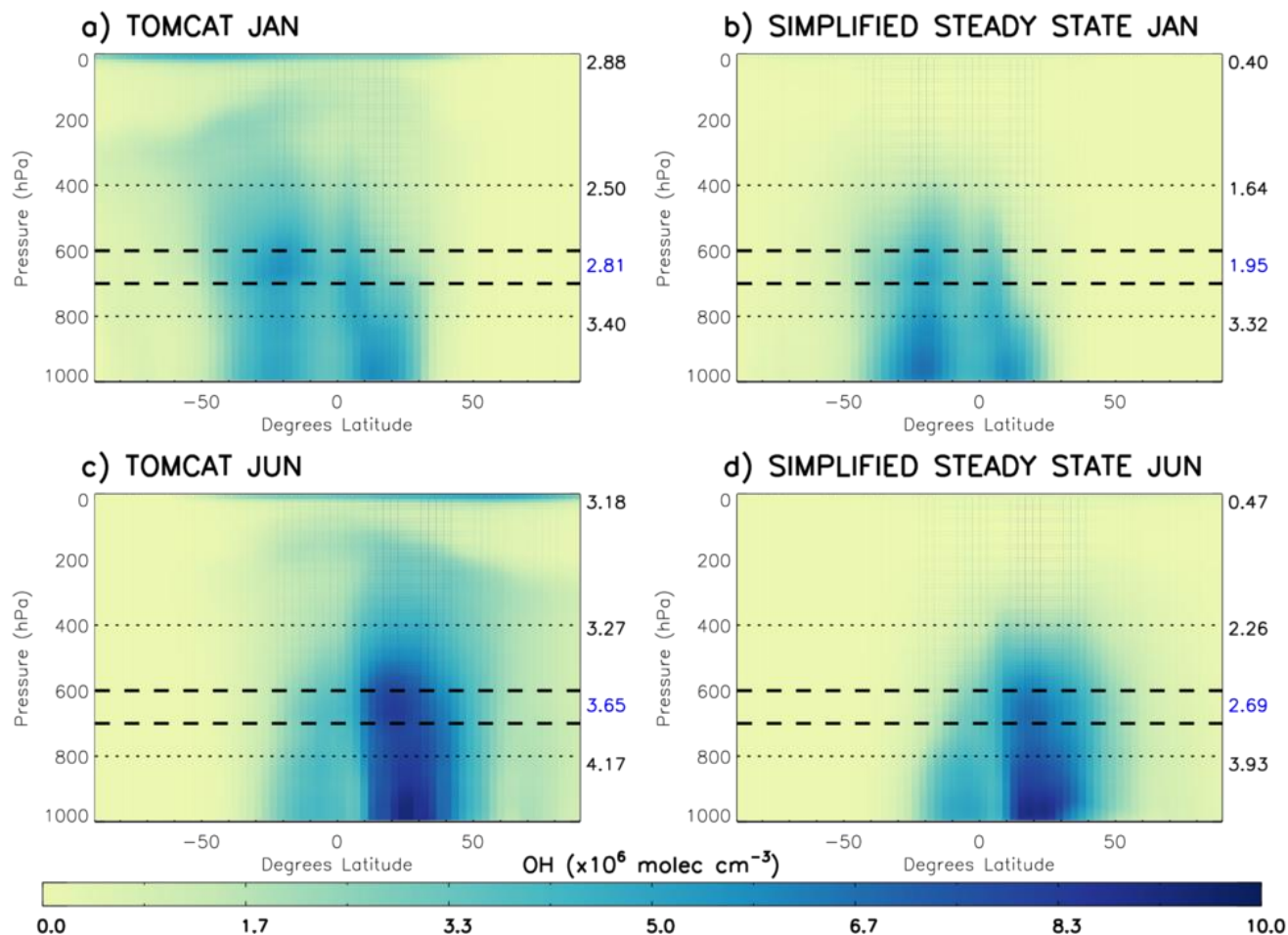
Figure 1: Comparison of TOMCAT OH and S-SSA OH in 2010: (a) TOMCAT OH January, (b) TOMCAT S-SSA OH January, (c) TOMCAT OH June, (d) TOMCAT S-SSA OH June. The dashed lines represent the proposed area of best agreement, 600–700 hPa. The numbers on the right of each plot represent the mass-weighted mean OH in $\times10^6$ molecule cm^{-3} of the region shown by the dotted lines (from top to bottom): < 400 hPa, between 400–800 hPa, between 800 hPa and the surface.

	S-SSA OH average – TOMCAT OH average ($\times10^6$ molecule cm^{-3})	
Pressure range	January	June
< 400 hPa	-2.48 (-86 %)	-2.71 (-85 %)
400–800 hPa	-0.86 (-34 %)	-1.01 (-31 %)
> 800 hPa	-0.08 (-6 %)	-0.24 (-2 %)
600–700 hPa	-0.86 (-31 %)	-0.96 (-26 %)

Table 1: Comparison of mass-weighted global mean TOMCAT OH and S-SSA OH for different pressure ranges. Percentage difference relative to the TOMCAT OH mean given in brackets.
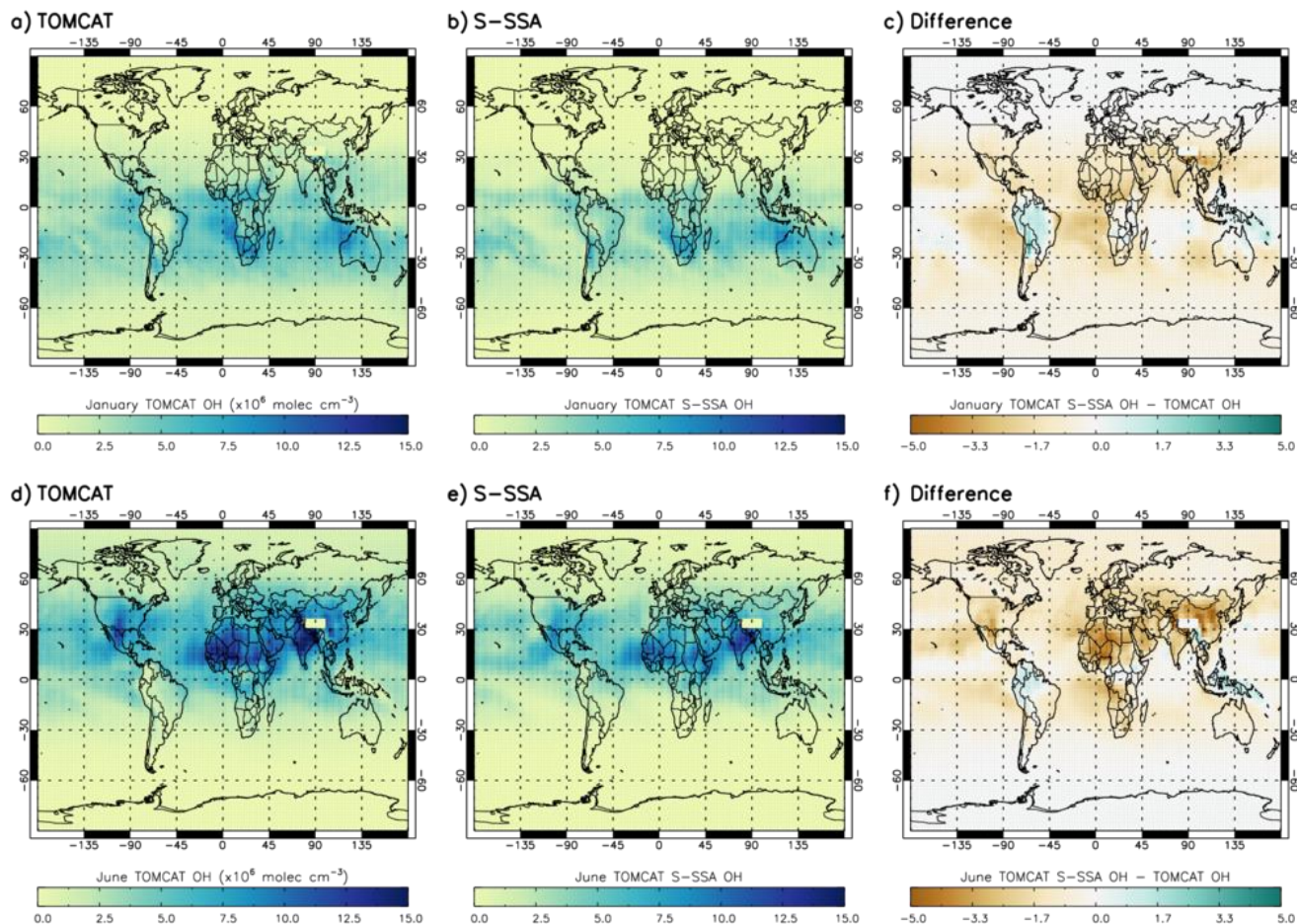
Figure 2: OH concentrations averaged over the 600-700 hPa range for TOMCAT, S-SSA and the difference (TOMCAT S-SSA minus TOMCAT). Panels a)-c) and d)-f) represent comparisons for January and June, respectively. All values are in in units of ×10⁶ molecule cm⁻³.

3.1.2 Study of reactions omitted from the S-SSA

The aim of this study is to derive information about OH from satellite data. Therefore, some source and sink reactions, which do not have relevant satellite retrievals, have been omitted from the S-SSA. We apply TOMCAT model data to another more complex steady-state approximations, Sav-SSA, to demonstrate which atmospheric species additional to H_2O, O_3, CO and CH_4 are key to OH production and removal in the pressure ranges, <400 hPa and >800 hPa. The results are shown as zonal means in supplement Sect. S8. Figures S11 and S12 show that the reaction of nitric oxide (NO) and the hydroperoxyl radical (HO_2) to be an important missing source at pressures <400 hPa. The OH and HO_2 radicals are closely linked in chemical cycles which are not, however, represented in the S-SSA.

Figure 3 shows the regional impact of the NO + HO$_2$ source term on the total production term of the Sav-SSA, averaged across the 600 – 700 hPa pressure layer. In areas with very high NO + HO$_2$ percentage contributions, it is likely that the S-SSA does not sufficiently capture all the important chemical pathways. For January, the NO + HO$_2$ source term shows a very large percentage contribution between 30°N and 60°N (up to 100%), although the [OH] is very low there and therefore relatively unimportant. Below 30°N, the spatial distribution of this percentage contribution is similar to the spatial distribution of the negative differences between TOMCAT and S-SSA [OH] in Fig. 2, indicating that these regions would have improved agreement with the addition of this source term. For example, across the NH oceans and continents and in the SH Atlantic and Pacific Ocean off the coast of S America. For June, the NO + HO$_2$ source term makes a larger percentage contribution across the SH oceans and continents (where [OH] is low). In the NH, the NO + HO$_2$ source term makes a greater contribution over land, and a very low contribution over the oceans, where Fig. 2 shows that the S-SSA [OH] is in good agreement with the TOMCAT [OH].

Figures S13 and S14 show a comparison between [OH] calculated using the S-SSA, as in Eq. (4), but with the addition of 1 source term (NO + HO$_2$) and 2 sink terms (NO + OH + M and NO$_2$ + OH + M). The [OH] calculated using the NO$_x$ terms shows an overestimate of between ~0 and 4 $\times 10^6$ molecule cm^{-3} compared to TOMCAT [OH] for both January and June 2010 and improves the agreement in some regions, such as at broadly above the equator in January and below the equator in June.

Although the NO + HO$_2$ source term is important in some regions, there are no NO or HO$_2$ satellite observations available in the relevant pressure range, so we cannot include this term in the S-SSA in this study. Introducing co-located tropospheric NO$_2$ satellite data from another instrument on MetOp-A, the Global Ozone Monitoring Experiment-2 (GOME-2), alongside IASI (Munro et al., 2016) is an area for potential future work. This would require additional steady-state balance expressions for NO:NO$_2$ and for HO$_2$.

a) Total Production

b) NO + HO₂ %

January Total Production Term (x10⁵)

0.0   16.7   33.3   50.0   66.7   83.3   100.0

January NO + HO₂ contribution to Production (%)

0.0   16.7   33.3   50.0   66.7   83.3   100.0

c) Total Production

d) NO + HO₂ %

June Total Production Term (x10⁵)

0.0   16.7   33.3   50.0   66.7   83.3   100.0

June NO + HO₂ contribution to Production (%)

0.0   16.7   33.3   50.0   66.7   83.3   100.0
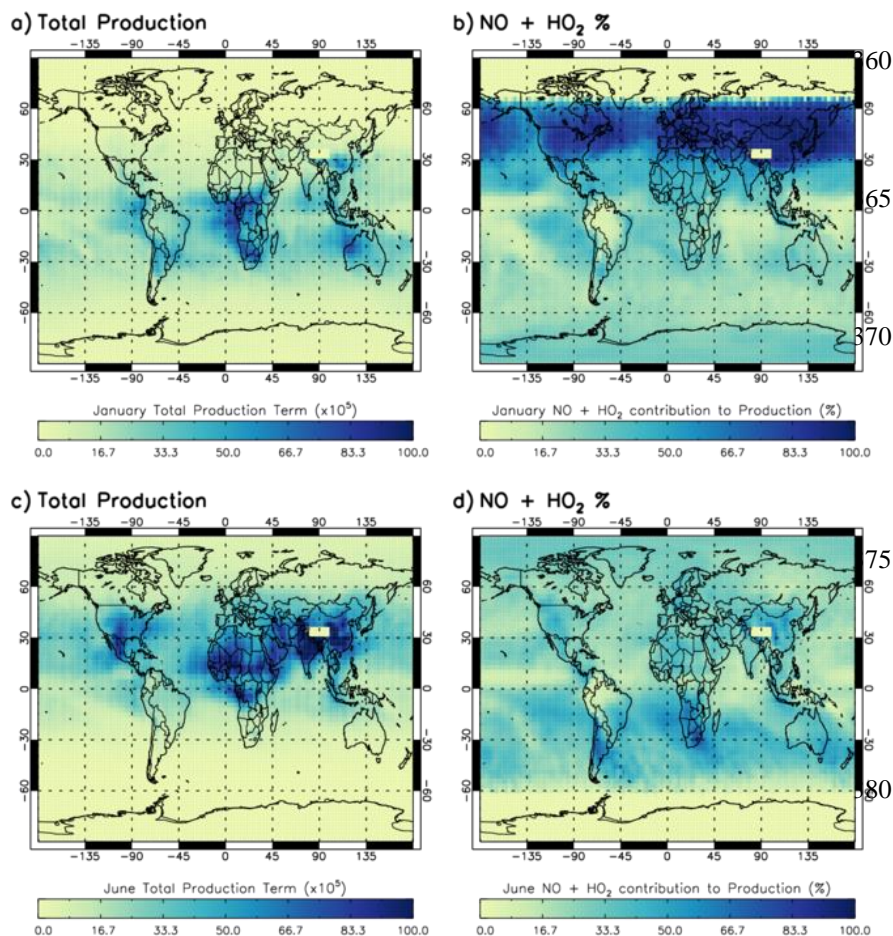
Figure 3: Contribution of NO + HO₂ reaction to total production term for Sav-SSA in 2010 averaged for the 600-700 hPa pressure region. (a) total production term in January, (b) percentage contribution of the NO + HO₂ source reaction to the total production term in January, (c) total production term in June, (d) percentage contribution of the NO + HO₂ source reaction to the total production term in June. Total production is in units of ×10⁵ molecule cm⁻³ s⁻¹.

385   Closer to the surface (> 800 hPa), Figs. S15 and S16 show that there are a number of important sink reactions for OH which are not included in the S-SSA, but are included in the Sav-SSA. These sink species include nitrogen dioxide (NO₂), dimethyl sulphide (DMS), hydrogen (H₂), hydrogen peroxide (H₂O₂), NO, sulphur dioxide (SO₂), formaldehyde (HCHO) and a combination of hydrocarbons (e.g. alkanes and alkenes).

390   Figure 4 shows the regional impact of two VOC terms (of interest) on the total production term of the Sav-SSA, averaged across the 600 – 700 hPa pressure layer. The regional contribution of all sink terms can be found in the Supplementary Material. Figure 4 shows that C₅H₈ (isoprene), from the sum of hydrocarbon term, shows a large contribution across South America and Indonesia in both January and June. These are regions of high S-SSA OH compared to TOMCAT OH seen in Fig. 2, representing the lack of this sink term in the S-SSA, leading to an overestimation by the S-SSA. In these regions, the

395   S-SSA expression is shown to not fully capture the OH chemistry. Formaldehyde (HCHO) represents ~10% of the total sink term in both months.

Figure 4: Contribution of isoprene (C₅H₈) and formaldehyde (HCHO) OH sink reactions to the total sink term for Sav-SSA in

2010 averaged for the 600-700 hPa pressure region. (a) Total sink term in January, (b) percentage contribution of the OH + C₅H₈ to the total sink term in January, (c) percentage contribution of the OH + HCHO to the total sink term in January, (d) total sink term in June, (e) percentage contribution of the OH + C₅H₈ to the total sink term in June, (f) percentage contribution of the OH + HCHO to the total sink term in June. Percentage value in panel label (i.e. 0-40 %) refers to the colour bar range. Total sink is in units of s⁻¹.
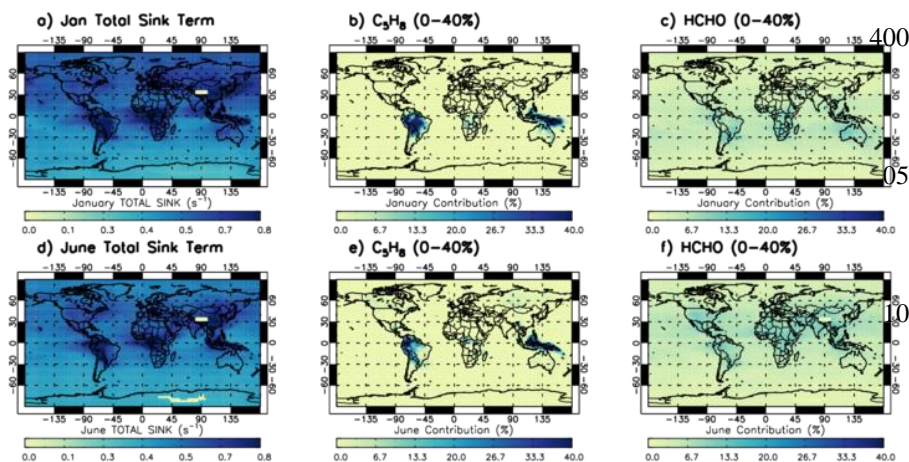
These additional source and sink terms could potentially help reduce the overestimate of the S-SSA in this region. Satellite data on tropospheric columns of NO₂ and several other relevant species (HCHO and SO₂ at enhanced levels) are available from GOME-2 alongside IASI on MetOp-A. Other than in tropical regions of lightning NOₓ production and rapid convective uplift, these reside principally in the lower troposphere. Co-located data from GOME-2 could therefore allow further investigation in future work. For the other source and sink species, satellite data is either not available in the relevant pressure region or not available from a similar instrument to the species in the S-SSA. This would yield problems, such as in combining observations with different vertical resolutions at different locations and times of day.

Overall, the spatially varying importance of different source and sink terms prevents the S-SSA from achieving a spatially uniform agreement and this must be considered when applying the approximation.

3.1.3 Application to satellite data

We apply satellite-retrieved trace gas data and model j_1 for 2010 to estimate [OH] using the S-SSA in the layer of interest, between 600–700 hPa. The satellite profiles interpolated to this layer are applied on an individual sounding basis for the daytime (~9:30 am local time) overpass. The [OH] estimates are then gridded onto the model grid for comparisons. Figure 5 shows the satellite S-SSA [OH] for 2010. The mass-weighted global mean [OH] ranges from 2.1×10^6 molecule cm⁻³ (January) to 2.9×10^6 molecule cm⁻³ (July). The seasonal variation is clear, with the higher [OH] values e.g. above 5.0×10^6 molecule cm⁻³ mostly in the SH during the summer (December-February), with a grid-box maximum value of 10.6×10^6 molecule cm⁻³. These larger [OH] concentrations in the tropical region, between 30° S–30° N, appear from March to May, with a grid-box maximum of 10.9×10^6 molecule cm⁻³. For June to August the higher [OH] values are mostly in the NH, with

a grid-box maximum of 28.1 ×10^6 molecule cm^{-3}. The higher [OH] values are present around the equator and sub-tropics in September to November, with a grid-box maximum of 11.4 ×10^6 molecule cm^{-3}.
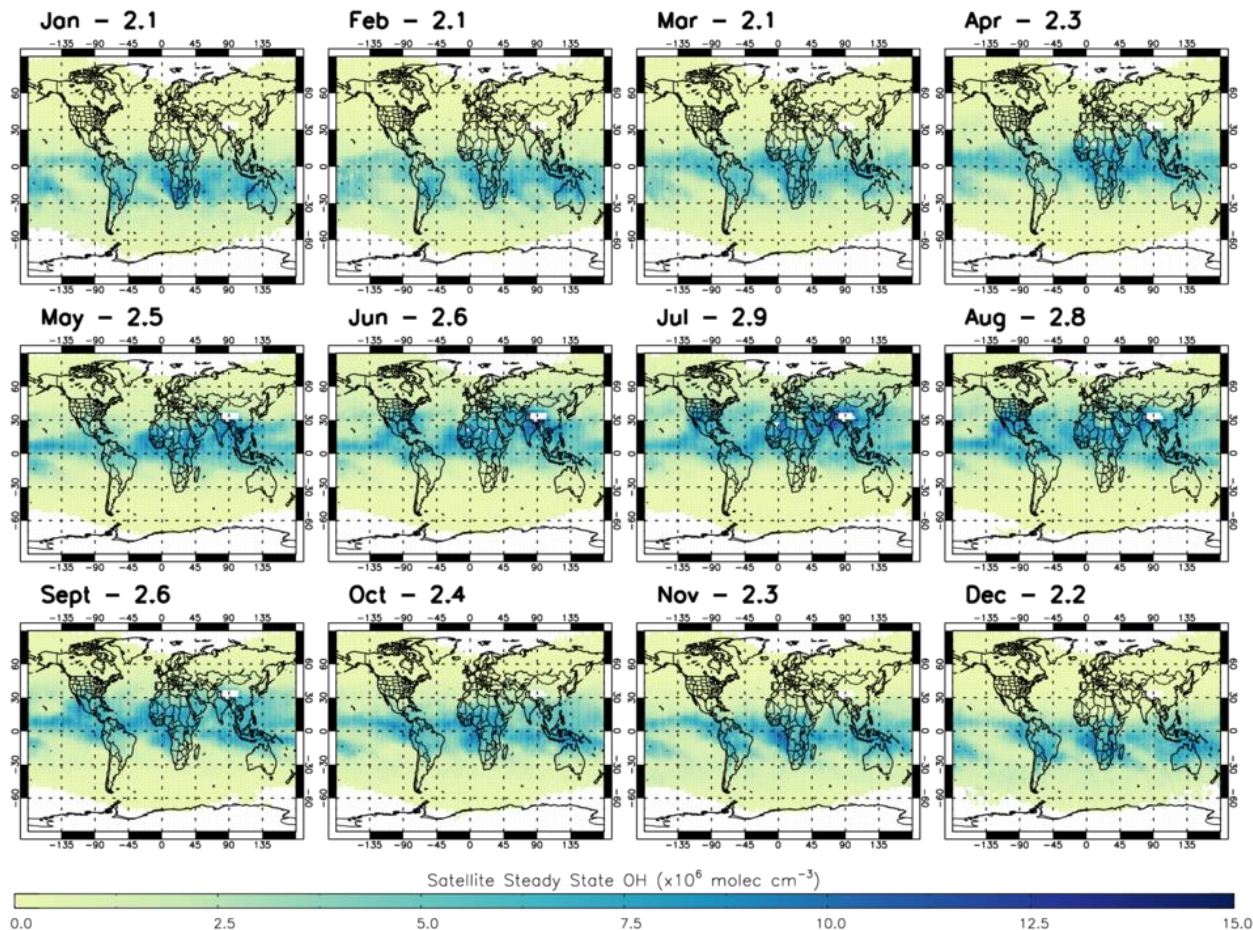
Figure 5: Satellite S-SSA OH (×10^6 molecule cm^{-3}) averaged for the 600–700 hPa layer in all months of 2010. Global mass-weighted mean OH values (×10^6 molecule cm^{-3}) for this region are labelled for each month.

Figure 6 shows a comparison of TOMCAT, TOMCAT S-SSA, TOMCAT FC-SSA and satellite S-SSA [OH] in January and June 2010. In both months the four estimates are seen to have very similar geographical structures. As expected, TOMCAT [OH] and TOMCAT FC-SSA [OH] show spatial patterns and global averages which are particularly similar (<6 % difference). This good agreement indicates that the use of monthly model data in the steady-state expression matches well with the numerical integration scheme inside the model. The TOMCAT and satellite S-SSA distributions also agree well in both months. The agreement is closer in January than June, with comparable peaks over NW Australia and S Africa with a TOMCAT [OH] grid-box maximum of 9.7 ×10^6 molecule cm^{-3} and a satellite [OH] grid-box maximum of 10.3 ×10^6 molecule cm^{-3}. The TOMCAT and satellite S-SSA January global mean [OH] values are 2.85 and 2.21 ×10^6 molecule cm^{-3},

450   respectively, so are consistent to ~22 %. In June 2010, TOMCAT and satellite S-SSA distributions have peaks over S Asia
and N Africa. Over SE Asia, the TOMCAT and satellite peaks are ~15 and 12 ×10^6 molecule cm^{-3}, respectively, and over N
Africa they are ~15 and 8 ×10^6 molecule cm^{-3}, respectively. The TOMCAT distribution also has a peak over N America
which is not captured by the satellite S-SSA. The TOMCAT and satellite S-SSA June global mean [OH] values are 3.80 and
2.73 ×10^6 molecule cm^{-3}, respectively, so are consistent to ~28 %. The correlation co-efficient between the monthly average
455   grid-boxes of TOMCAT and satellite S-SSA OH is 0.85 for January and 0.83 for June. In summary, the monthly-mean
geographical distributions and global averages derived using the S-SSA (using TOMCAT/satellite data) agree well with
those from TOMCAT and TOMCAT FC-SSA, indicating the S-SSA offers a useful approach to investigate [OH] behaviour
globally in the 600–700 hPa layer. The monthly-mean distributions of satellite-derived S-SSA [OH] agree well with
TOMCAT S-SSA although values are generally lower, indicating some inconsistency between TOMCAT and satellite in the
460   distributions of H_2O, O_3, CO and/or CH_4. The same analysis was applied to data from 2017 (Fig. S10) and similar results
obtained, a global underestimate for the satellite S-SSA of 21 % in January and 28 % in June.

3.1. Application to aircraft data

To further assess the robustness of the S-SSA, we apply it to CH_4, CO, O_3, H_2O and j_1 observations from four ATom
465   campaigns. Figure 7 shows a comparison between [OH] observed by ATom (OH-obvs) and as calculated from ATom H_2O,
O_3, CO and CH_4 observations using the S-SSA (OH-calc) where ATom data were available for all species. Across all four
ATom campaigns, OH-calc is biased by -25.8 % with respect to OH-obvs. This bias is similar to the uncertainty on OH-obvs
of ~35 % (Brune et al., 2020). For the four individual campaigns, the % bias is persistently negative, ranging from -21.1 to -
25.2 % for ATom-1,3,4 and -48.8 % for ATom-2. One explanation for the large normalised mean bias for ATom-2 is due to
470   the predominance of smaller values of [OH] during this campaign, leading to higher percentage differences, as the absolute
bias is more in line with the other campaigns. Across the four campaigns the Pearson's correlation co-efficient is 0.78, and
for the four individual campaigns, the correlation ranges from 0.51 to 0.86.

Figure 8 shows a comparison between zonally-averaged OH-obvs and OH-calc. The left panels show that for OH-obvs, the
475   higher values are predominantly found closer to the equator although exceptions exist e.g. around 45°N in ATom-1. The
right panels show that for the majority of latitudes, OH-obvs is larger than OH-calc across all four campaigns, with a few
exceptions, mostly in ATom-2 and 4. The deviations range from -9.7 ×10^6 molecule cm^{-3} to 4.1 ×10^6 molecule cm^{-3}.
Generally, they are smallest between 30° S and 90° S, corresponding to the low OH-obvs and OH-calc values in this region.
They are higher in 30° S–30° N and 30°–90°N, corresponding to generally higher OH-obvs and OH-calc values near the
480   equator and some large values in the NH mid-latitudes.

The normalised mean bias between OH-obvs and OH-calc is ~26 % which is a similar order of magnitude to the large uncertainty of 35 % for the OH observations. The ATom observations provide a comparatively large aircraft dataset for comparison, however, it nonetheless has a limited spatiotemporal extent, which must be acknowledged when interpreting our results. Here, we believe that for the observations used, the datasets are correlated sufficiently to justify further study of the S-SSA at this pressure range.

As the normalised mean bias between OH obvs and OH calc is comparable to the uncertainty on the OH obvs and the datasets are well correlated, this analysis of the ATom campaigns provides further justification that the use of the S-SSA to further study OH in this pressure range is robust.
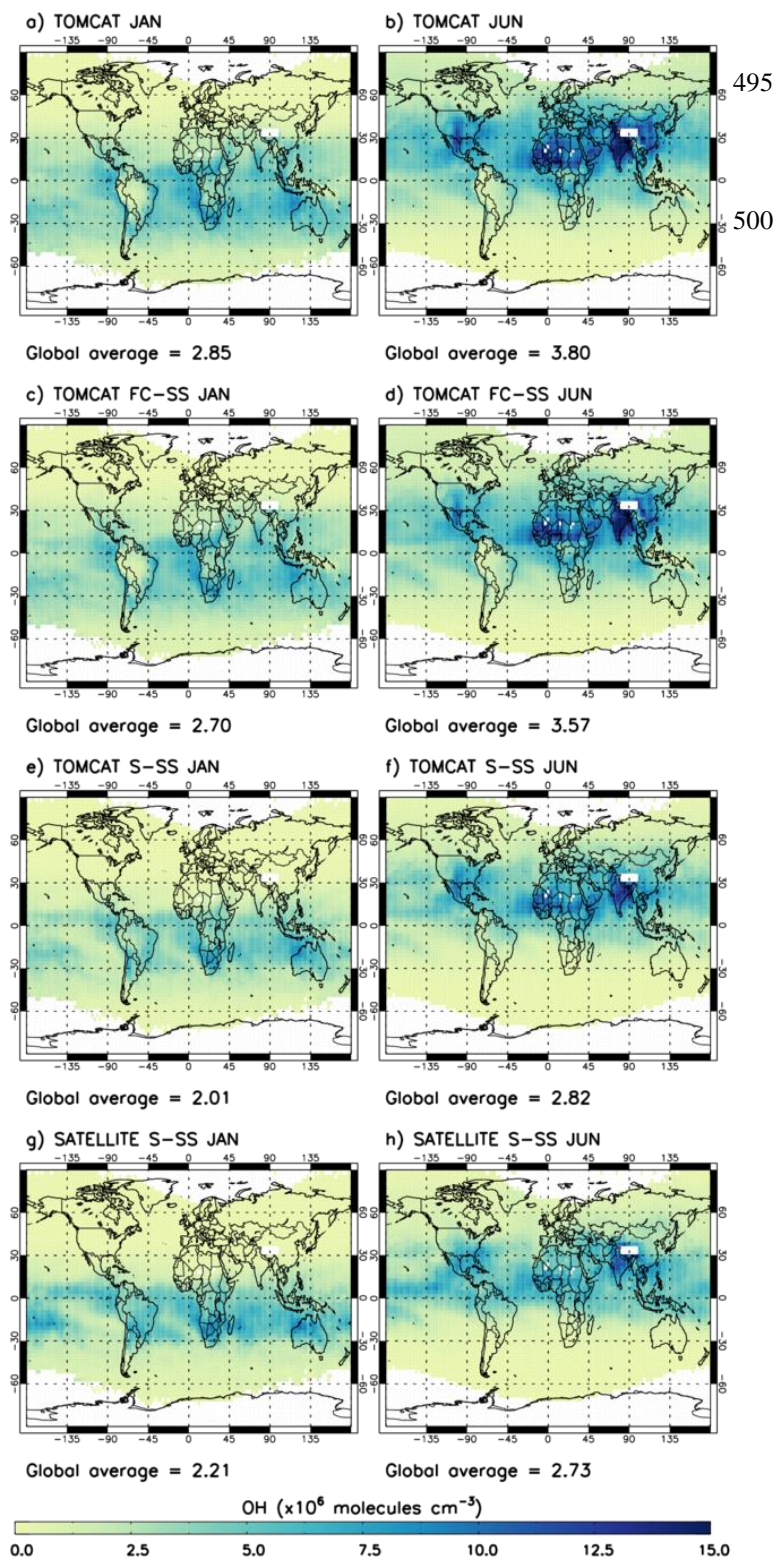
Figure 6: 2010 OH comparison in the 600–700 hPa layer: (a) TOMCAT January, (b) TOMCAT June, (c) TOMCAT FC-SSA January, (d) TOMCAT FC-SSA June, (e) TOMCAT S-SSA January, (f) TOMCAT S-SSA June, (g) Satellite S-SSA January and (h) Satellite S-SSA June. Global mass-weighted mean OH values (×10⁶ molecule cm⁻³) for this atmospheric region are given below each panel.
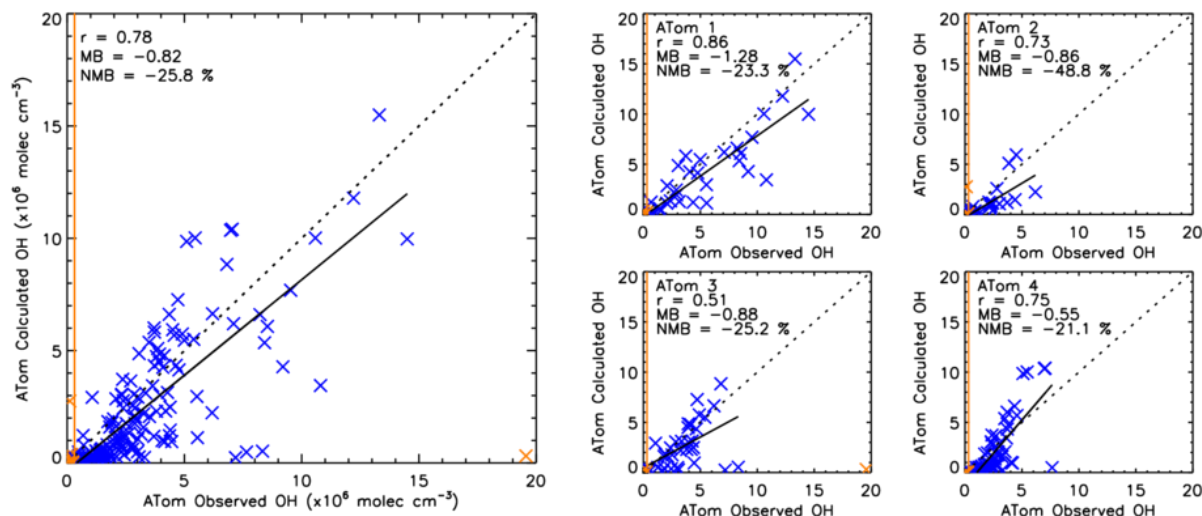
Figure 7: Comparison between OH-calc and OH-obvs. The left panel shows a combination of ATom-1, ATom-2, ATom-3 and ATom-4. The right four panels show the data split into the individual campaigns. ATom observations are filtered for 600–700 hPa and 08:00–11:00 LT. All data is in units of ×10⁶ molecule cm⁻³. Data points in orange are excluded from the analysis, either as an outlier (> mean + 3.0 standard deviations) or below the limit of detection of the ATHOS instrument (0.018 pptv or 0.31 ×10⁶ molecule cm⁻³) shown by the orange line. Pearson's correlation co-efficient (r), the mean bias (calculated from OH-calc – OH-obvs) and the normalised mean bias (% with respect to OH-obvs) are displayed in the top left corner of each panel.

Figure 9 shows OH-obvs overlayed onto a satellite derived [OH] field averaged across the corresponding days in 2017. The comparison is challenging due to the sparse nature of the ATom data points compared to the satellite [OH] field (highlighted in Fig. 9) and using satellite data only for 2017 (ATom-1 occurred in 2016 and ATom-4 in 2018). There are examples of good agreement between the satellite and OH-obvs in some peak [OH] regions, e.g. off the western coast of Mexico between the equator and 30° N in ATom-1, and also low [OH] regions, e.g. over the North Atlantic ocean in ATom-2. However, there are also examples of poor agreement, e.g. high values in OH-obvs near Alaska and low values in the satellite OH in ATom-3 and 4. Across the four campaigns, the correlation co-efficient ranges from 0.15 to 0.75, and the bias of satellite with respect to ATom ranges from -60.1 % to -35.1 %. ~~Figure 6 highlights the sparse nature of the ATom data in comparison to the satellite [OH] field.~~The poor comparison in some regions may be attributable to the resolution difference between the point aircraft observations and the averaged satellite [OH] field, due to spatial inhomogeneity of OH.

Figure 10 shows a comparison between OH-obvs and the nearest value from the averaged satellite [OH] field (OH-sat). The data is coloured by latitude and, as in Fig. 9, indicates OH-sat to be negatively biased with respect to OH-obvs at northern mid–high latitudes, but to a lesser extent at lower latitudes. Across the four campaigns, the values at northern mid–high latitudes (30°–90° N) and the values at lower latitudes (90° S–30° N) show similarly high correlation co-efficients of 0.68, with a small difference of 9.4 % for the lower latitudes, and a much larger difference of 72.8 % for the higher latitudes. This

corresponds to the results in Sect. 3.1.2, where the OH source reaction $HO_2 + NO$ represents a larger contribution to the total production in the NH high latitudes in winter (ATom-2,3,4). The reduction in agreement in this region, indicates that the S-SSA may not be able to provide robust information about [OH] here. In Sect. 3.3 we study a tropical (15° S–15° N) band, where the S-SSA shows a more robust agreement.

530
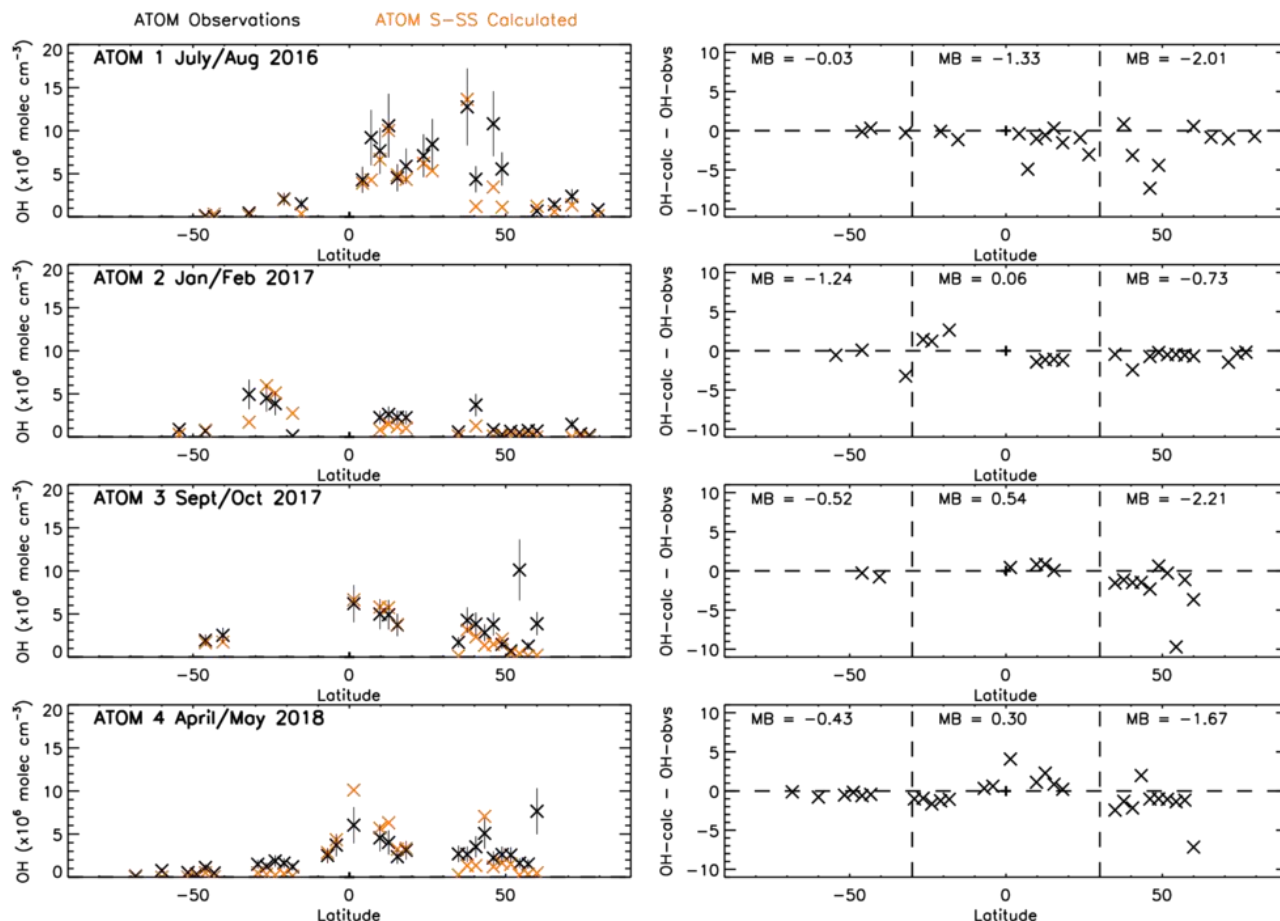
Figure 8: OH-calc and OH-obvs comparison. Left panels show latitude-averaged OH (ppt) with error bars of 35 %. Right panels show latitude-averaged OH difference between OH-calc and OH-obvs (calc – obvs) with the mean difference (MB) labelled for 3 different latitude regions marked by the dashed lines (90°–30° S, 30° S–30° N and 30°–90° N). All data is in units of ×10⁶ molecule cm⁻³. ATom observations are filtered for 600–700 hPa and 08:00–11:00 LT.

535

3.1.5 Aircraft data and omitted source terms

Fig. S17 is similar to Fig. 7 but shows a comparison of ATom OH-calc with (OH-calc-NO_x) and without (OH-calc) 3 NO_x reactions ($NO + HO_2$, $NO + OH + M$, $NO_2 + OH + M$) included in the S-SSA. The addition of the NO_x terms changes the

540   bias in the OH-calc relative to OH-obvs from -20.6 % to +13.2 %. This change in sign is consistent with the comparison of S-SSA and S-SSA with NO_x reactions using model data as shown in Figs. S13 and S14. Overall, the correlation remains similar for with and without NO_x (0.76 and 0.78). This corresponds to the model results in Sect. 3.1.2 which show that for some regions, the $NO + HO_2$ source term can make a large contribution to the total source term.

3.2 OH reactivity

As described in Sect. 2.2, OHR observations can potentially be used to check the denominator of a steady-state approximation, in this case a simplified expression of OHR (Eq. (5)). Supplementary Sect. S10 (Figs. S18 and S19) discusses our comparisons between ATom OHR observations (OHR-obvs) and ATom data used in the simplified expression for OHR (OHR-calc). Although ~80 % of calculated OHR values fell within the range of measurement uncertainty, the estimated error on OHR measurements (0.8 s^{-1}) was too large to find any correlation with calculated OHR (r = -0.02). The bias in calculated OHR varied between -57 % to +20 % over the four campaigns and the average bias in calculated OHR (-37 %) over the four campaigns (Fig. S18) is compatible with the (-28 %) bias in S-SSA [OH]. Several studies (Thames et al., 2020; Travis et al., 2020) have quantified "missing OH reactivity" in the boundary layer in detail, however, our analysis of ATom [OH] and OHR measurements demonstrates the S-SSA to estimate [OH] with an accuracy within ~30% in the 600–700 hPa layer.

3.3 OH temporal variation

Satellite data in conjunction with the S-SSA presented in previous sections provides a mean to examine the temporal variation in global [OH]. We use satellite data produced on a sub-sampled basis from 2008–2017 and the S-SSA, together with fixed ~~annual~~ monthly model j_1 distributions from the TOMCAT model for a fixed year (2010). The use of a fixed year of j_1 distributions removes any influence from variation in this value between years e.g. from variation in overhead stratospheric ozone, which is an assumption that should considered when interpreting these results. Figure 11 shows the time series of global, NH, SH and tropical (15° S–15° N) OH monthly anomalies with respect to the 2008-2017 mean for each month for the 600–700 hPa layer. We include a tropical band as this is the most representative region of OH using the S-SSA. Similar plots in Sect. S11 show % anomalies for the input species and temperature (Figs. S20–S24). During this time period the [OH] anomaly varies between: -0.10 and +0.15 $\times 10^6$ molecule cm^{-3} for the global average; -0.15 and +0.11$\times 10^6$ molecule cm^{-3} for the NH average; -0.21 and +0.21 $\times 10^6$ molecule cm^{-3} for the SH average; and -0.37 and +0.54 $\times 10^6$ molecule cm^{-3} for the tropical average. Aside from a few exceptions, the global, NH, SH and tropical average follow a similar pattern. Notable positive anomalies (values given for the tropical band, in units of $\times 10^6$ molecule cm^{-3}) occur in mid-2010 (+0.30), the end of 2012 and beginning of 2013 (+0.54), mid-2015 (+0.15) and mid-2016 (+0.14). Notable negative anomalies occur in mid-2009 (-0.27), 2011 to mid-2012 (-0.37), end of 2015 and beginning of 2016 (-0.21) and the end of 2017 (-0.22). The global annual mean [OH] anomaly ranges from -3.1 % to +4.7 % and the tropics anomaly ranges from

around -6.9 to +7.7 %. This behaviour is broadly similar to other studies of [OH] variability using MCF observations and chemistry transport models, which find a range of around -6 to +6 % for global [OH] anomaly during this time period (although our assessment is limited to a specific pressure range, so this is not a direct comparison) (Voulgarakis et al., 2015;

575   Patra et al., 2021).

Figure 12 shows contrasting behaviour of the three sink terms during the time period 2008–2017. It shows that in the 600–700 hPa layer, CO is the dominant sink term, ranging between 0.20–0.45 s^{-1}, with the CH_4 sink having the next largest contribution between 0.10–0.15 s^{-1} and the O_3 sink having the smallest contribution at around 0.04 s^{-1}. The comparatively

580   large size of the CO sink, indicates that variation in CO is likely to dominate the variation in the total sink term. The CO sink is consistently lower in the SH than NH, with largest difference (~0.2 s^{-1}) in the first half of the year. The CH_4 and O_3 sinks show negligible difference between SH and NH, therefore the CO sink will have a lower percentage contribution in the SH. These findings are consistent with those from aircraft measurements below 3 km in Travis et al. (2020) and from model data in the free troposphere in Lelieveld et al., (2016). Satellite CH_4 shows a positive trend of 4.5 ppb yr^{-1} throughout this time

585   period (Fig. S21). However, as seen in Fig. 12, when the rate constant is applied, the CH_4 sink term shows very little variation, with no evidence of the positive trend in CH_4 concentrations having a significant impact. The source term (numerator of Eq. (4)) varies between 5–15 $\times 10^5$ molecule cm^{-3} s^{-1} for the global, NH and SH averages, while for the tropical band it ranges between 15–28 $\times 10^5$ molecule cm^{-3} s^{-1}.

590
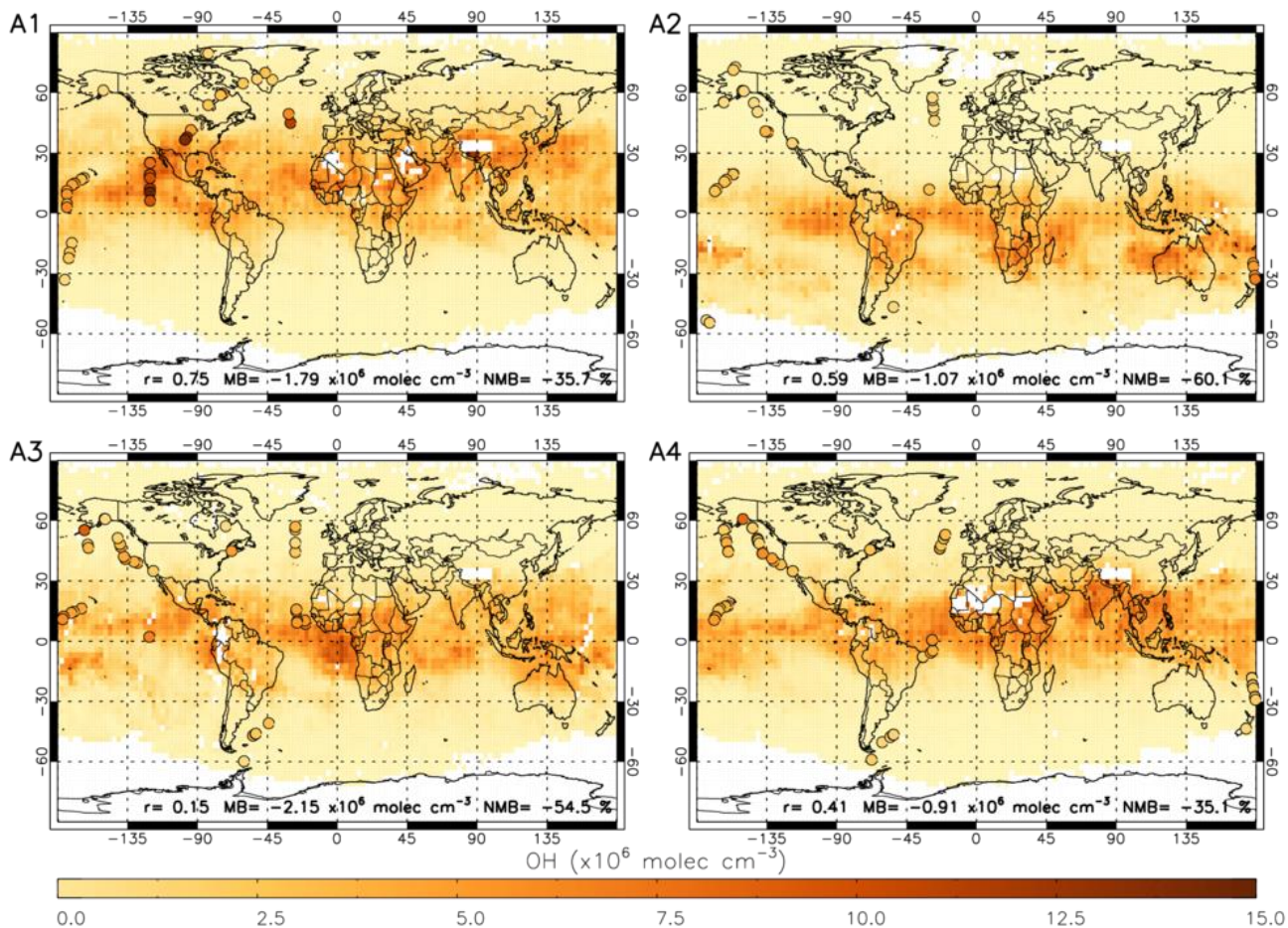
Figure 9: Satellite OH for four periods in 2017 corresponding to A1 to A4 (ATom-1 to ATom-4, 2016-2018) with ATom OH observations (OH-obvs) overlaid on top as coloured circles. ATom observations are filtered for 600–700 hPa and 08:00–11:00 LT. The Pearson's correlation co-efficient (r), mean bias (calculated from the nearest satellite grid cell – OH-obvs) and the normalised mean bias (% with respect to OH-obvs) are displayed at the bottom of each panel. All data is in $\times 10^6$ molecule cm^{-3}.
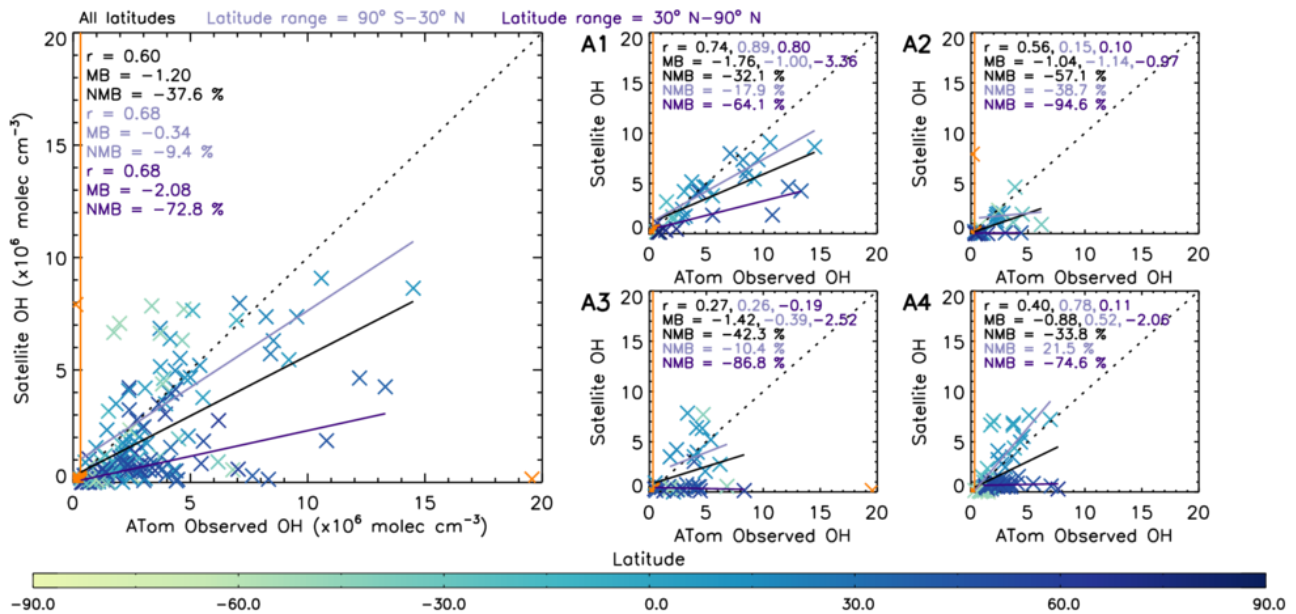
Figure 10: Comparison between OH-obvs and OH-sat (nearest satellite OH value to ATom observation from averaged 2017 satellite OH grid). The left panel shows a combination of ATom-1, ATom-2, ATom-3 and ATom-4. The right four panels show the data split into the individual campaigns. ATom observations are filtered for 600–700 hPa and 08:00–11:00 LT. All data are in units of $\times10^6$ molecule cm^{-3}. Data points in orange are not included in analysis, either as an outlier (> mean + 3.0 standard deviations) or below the limit of detection of the ATHOS instrument (0.018 pptv or 0.31 $\times10^6$ molecule cm^{-3}) shown by the orange line. Pearson's correlation co-efficient (r), the mean bias (calculated from OH-sat – OH-obvs) and the normalised mean bias (% with respect to OH-obvs) are displayed in the top left corner of each panel for 3 different latitude ranges: all latitudes, 90° S–30° N and 30°–90°N, respectively. The values are coloured by latitude as shown on the colour bar.

Figure 13 shows the temporal anomaly, relative to the 2008–2017 mean, of the balance between source and sink terms in the approximation and the derived OH concentration. The positive anomalies in mid-2010, end of 2012 and beginning of 2013, mid-2015 and mid-2016 coincide with the positive anomalies in the source term, driven by O_3 (O_3 anomalies are shown in Fig. S23), and smaller or close to zero anomalies in the sink terms. The negative anomalies in mid-2009, 2011 to mid-2012, and end of 2017 can be explained by a negative anomaly in the source term, again driven by O_3, and a small or close to zero anomaly in the sink term. The negative anomalies at the end of 2015 and beginning of 2016 can be explained by a very large positive sink term anomaly, despite the large positive source term anomaly. This large positive anomaly in the sink term corresponds to a large positive anomaly of CO in most latitudes (Fig. S22), with maximum anomaly ~12 % globally and ~20 % in the tropics. The 2015–2016 El Niño event is the likely cause of this CO anomaly, due to a large increase in global fire emissions (Huijnen et al., 2016). As shown in Fig. 13d, the event started at the end of 2014, peaked at the end of 2015 with a maximum Multivariate ENSO Index (MEI.v2) value of +2.2, and ended in May 2016 (Liu et al., 2017; NOAA, 2021). Biomass burning was also found to be the key driver of OH variability in a study by Voulgarakis et al. (2015).
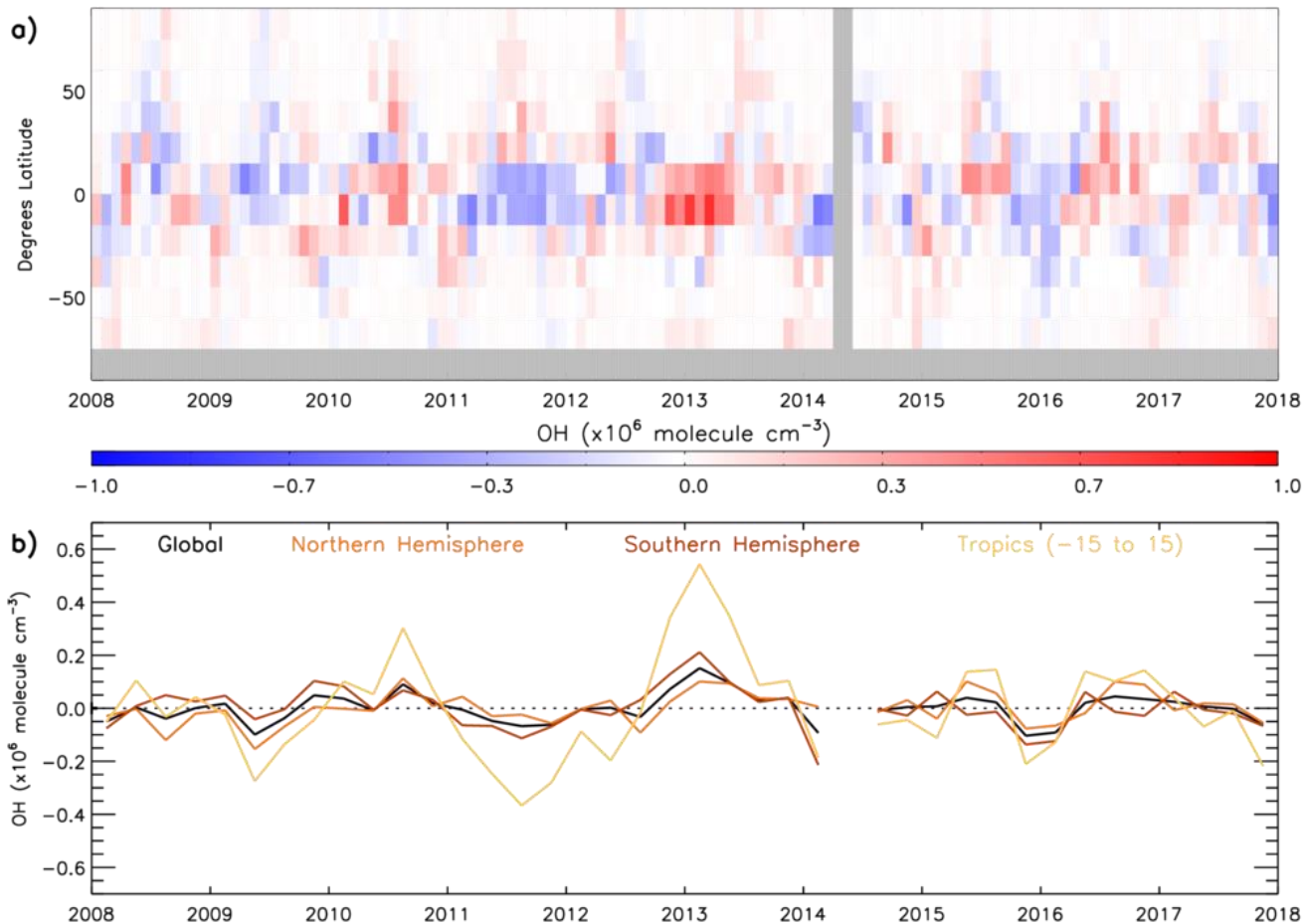
Figure 11: Monthly mean satellite OH anomaly (2008–2017): (a) 15° latitude bins and (b) 3-month average global, NH, SH and tropics means. All data is in ×10⁶ molecule cm⁻³. Anomaly is relative to a 2008–2017 average.

As the combined source term is a dominant driver of OH variability, it is useful to distinguish the relative importance of O_3 and water vapour in driving this variability. To do this, we repeat the source term calculation (numerator in Eq. (4)) but using a fixed value of O_3 or water vapour, respectively. These fixed values are derived from the average value for each month across the full 2008–2017 time series. If the source term anomaly time series derived using a fixed water vapour value can reproduce the original anomaly time series (i.e. Fig. 13b), this would demonstrate that variability of water vapour is not important in comparison to that of O_3 or vice versa (Fig. 14). Our results show that when water vapour is fixed (varying O_3) in the source term anomaly, 66.4 % of the variability (i.e. $R^2=0.664$) in the original source term can be explained on the global scale (Fig. 14c). When O_3 is fixed to a constant monthly value (varying water vapour), the R^2 value drops to 0.164 with only 16.4 % of the variability in the original source term anomaly explained by this time series (Fig. 14b). This demonstrates that variations in O_3 are the primary driver in the source term and therefore in the OH variability using the S-

SSA in this altitude range and time period. Cross-correlations between the drivers of the key species e.g. OH, O_3, are likely to exist, however a detailed analysis and quantification of this is beyond the scope of the study.

635
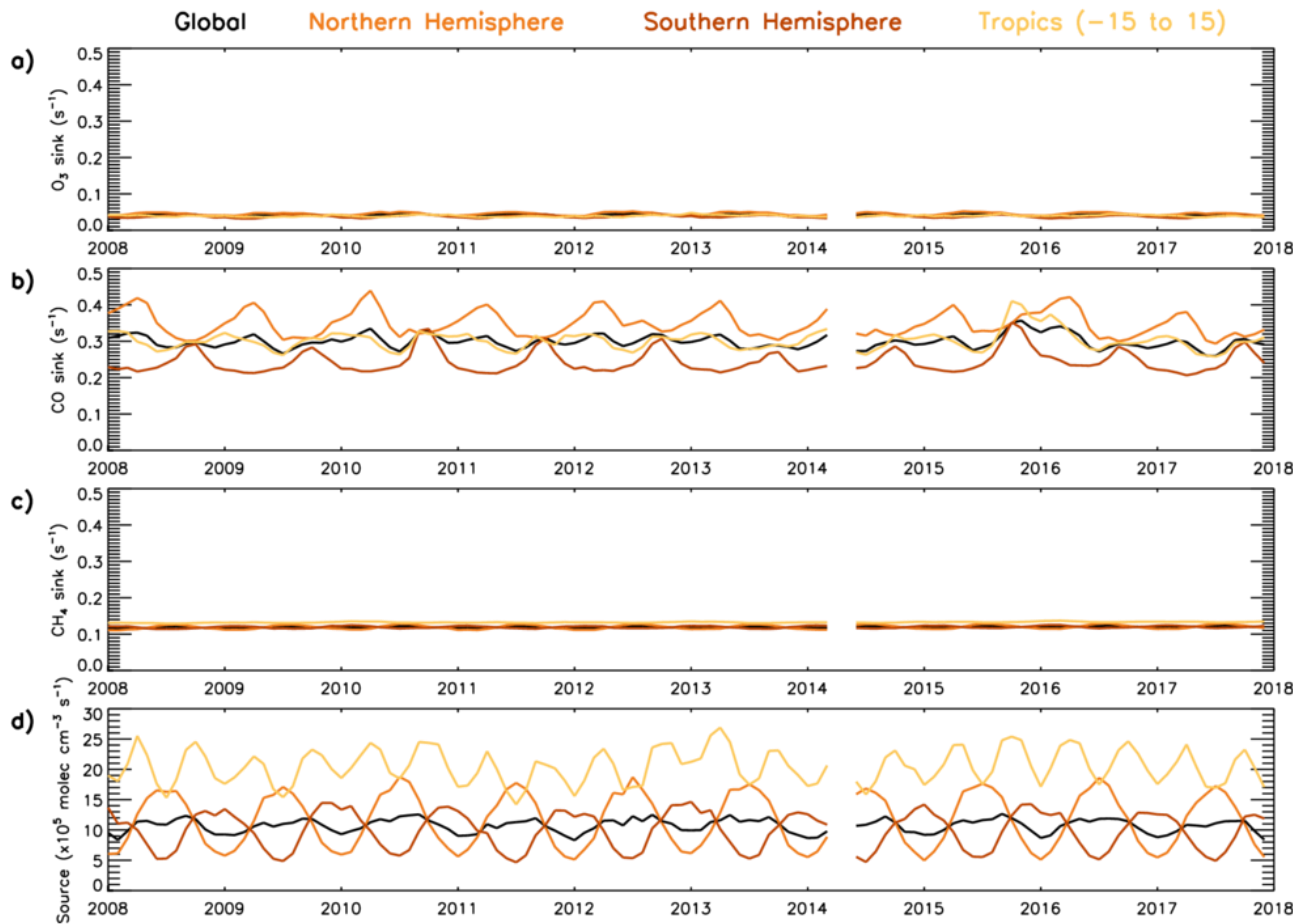
Figure 12: Temporal variability in the components of the S-SSA approximation (2008–2017). Global, NH, SH and tropical average time series for: (a) $k_{O_3+OH}[O_3]$, (b) $k_{CO+OH}[CO]$, (c) $k_{CH_4+OH}[CH_4]$ and (d)
640 **$2j_1k_1[O_3][H_2O]/(k_{N_2+O(1D)}[N_2]+k_{O_2+O(1D)}[O_2]+k_{H_2O+O(1D)}[H_2O])$.**
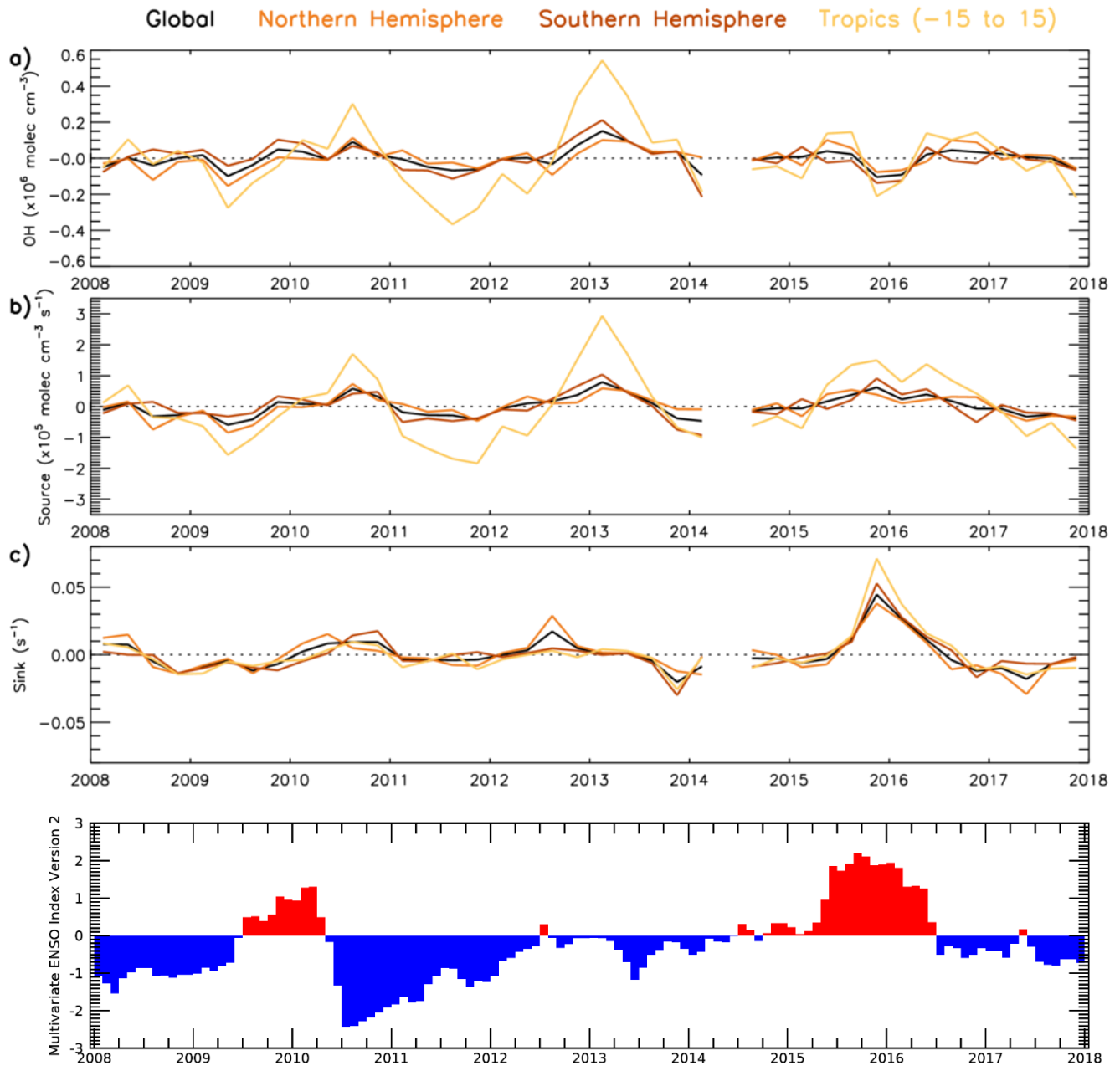
Figure 13. Temporal variability in OH anomaly and anomalies of the numerator (source) and denominator (sink) lines of the steady-state approximation in Eq. (4) (2008–2017). Global, NH, SH and tropical average time series for: (a) OH anomaly, (b) $2j_1[O_3][\ H_2O]/(k_{N2+O(1D)}[N_2]+k_{O2+O(1D)}[O_2]\underline{+k_{H2O+O(1D)}[H_2O]})$ (total source term) anomaly, (c) $k_{CO+OH}[CO]$ + $k_{CH4+OH}[CH_4]$ + $k_{O3+OH}[O_3]$ (total sink term) anomaly and (d) Bimonthly Multivariate ENSO index (NOAA, 2021). Anomalies are relative to a 2008–2017 average.
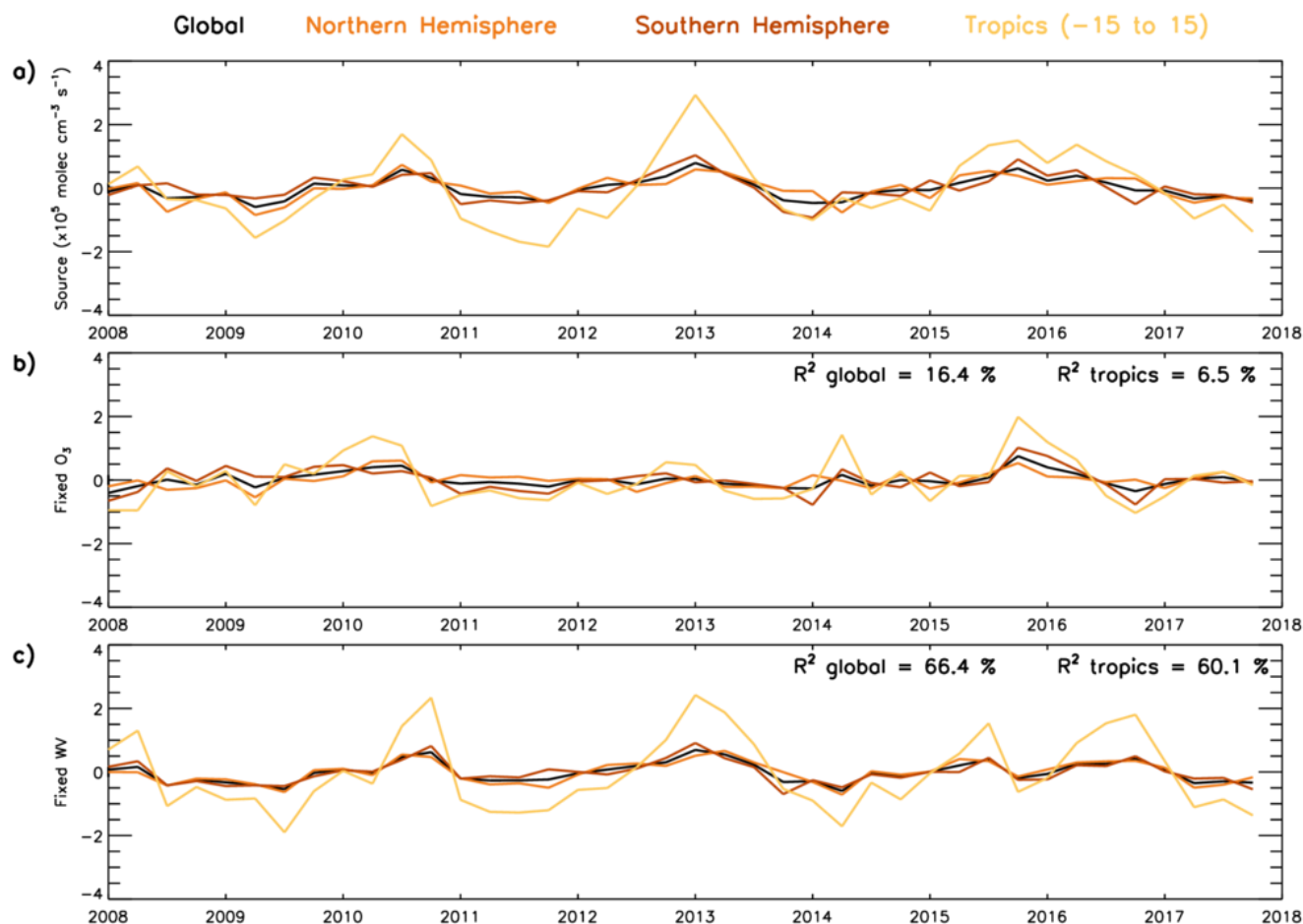
Figure 14. Global, NH, SH and tropical average time series (2008–2017) for: (a) OH S-SSA source anomaly, (b) OH S-SSA source anomaly calculated with fixed monthly O₃ concentrations (source fixed-O₃) and (c) OH S-SSA source anomaly calculated with fixed monthly water vapour concentrations (source fixed-wv). Fixed O₃/water vapour calculated as monthly average across the time period. Anomalies are relative to a 2008–2017 average. Values in the top right of panel (b) represent the R^2 value between the OH S-SSA source anomaly and the source fixed-O₃ anomaly and in the top right of panel (c) represent the R^2 values between the OH S-SSA source anomaly and the source fixed-wv anomaly. All data is in units of $\times10^5$ molecule cm^{-3} s^{-1}.

4 Conclusions

Due to its short photochemical lifetime, steady-state approximations are able to represent tropospheric OH concentrations well, depending on the complexity of the expression used and the atmospheric pressure range over which they are applied. The terms in the steady-state approximation also allow us to quantify components which contribute to the OH budget. A simplified steady-state approximation (S-SSA) can be constructed which contains terms based on trace gases observed by satellite. Results from the TOMCAT 3D chemical transport model show that this should be a good approximation to [OH] in the 600–700 hPa layer in terms of magnitude (~26–31 % underestimate in the mass-weighted global mean [OH] comparison

to full chemistry) and spatial distribution. This atmospheric layer is above the boundary layer where [OH] is substantially affected by many pollutants which are not measured by satellite and therefore invalidate the S-SSA. We have tested the S-SSA in the 600–700 hPa layer using data from four ATom aircraft campaigns and found that it tracked measured [OH] with a correlation of r = 0.78 and a mean bias of ~26 %, similar to the 35 % estimated uncertainty on the OH observations. Measurements of OH reactivity (OHR) allow the denominator of the S-SSA expression to be considered in addition and found to be consistent with an S-SSA [OH] accuracy of ~30 % in the 600–700 hPa layer.

The S-SSA approach allows us to demonstrate how a multi-year record of satellite observations can be used to examine interannual variability in tropospheric [OH]. Using H_2O, O_3, CO and CH_4 data retrieved from MetOp-A observations for 2008-17 we find the global annual mean [OH] anomaly to range from -3.1 % to +4.7 %. The influence of important terms in the OH budget was also derived, demonstrating the balance between the source and sink terms over time. Variation in the S-SSA OH was found to be determined primarily by the combined source term, driven by O_3, and by the CO sink term. In the tropics, OH variation reflected that of O_3 (peaks in 2008, 2010 and the largest in 2013) along with the positive CO anomaly associated with the strong El Niño event in 2015/16. Overall, we have demonstrated a novel and robust methodology, using satellite observations and a simple steady-state approach, to estimate mid-troposphere [OH], which can complement existing methods to measure [OH] (i.e. the limited network of surface sites, infrequent flight campaigns and the MCF-type approach to estimate global mean [OH]). Most importantly though, the approach here will provide the scientific community with a global observational constraint on mid-tropospheric [OH] and help future studies assess the [OH] impacts on important air quality (e.g. O_3 and NO_2) and climate (e.g. CH_4) trace gases.

Data availability. The ATom data (Wofsy et al., 2018) is available from: https://daac.ornl.gov/ATOM/campaign/. The MEI.v2 data (NOAA, 2021) is available from: https://psl.noaa.gov/enso/mei/. Satellite data was produced from MetOp-A with RAL's extended Infrared and Microwave Sounding scheme and IASI methane scheme (Siddans et al., 2020) are available at these locations respectively: http://homepages.see.leeds.ac.uk/~eemap/RAL_IASI_IMS_DATA/ (follow /FULLY_PROCESSED/ for the fully sampled data (2010 and 2017) and /PARTIALLY_PROCESSED/ for the sub-sampled data (2007–2018)) and http://dx.doi.org/10.5285/f717a8ea622f495397f4e76f777349d1.

Author contribution. MAP, MPC, RJP and BJK conceptualised and planned the research study. MAP and RP performed the TOMCAT model simulations with support from MPC and WF. MAP analysed the satellite data provided by RAL Space (BJK, RS, BGL, DSK and LJV) with support from RP and BJK. MAP undertook the ATom analysis and OH temporal variation analysis. RJP compared the IMS O_3 to ozonesondes. MAP created the plots and prepared the manuscript with contributions from RJP, MPC, DEH and BJK.

Competing interests. The authors declare that they have no conflicts of interest.

Acknowledgements. This work was undertaken on ARC3, part of the High Performance Computing facilities at the University of Leeds, UK. This work was supported by the Panorama Natural Environment Research Council (NERC) Doctoral Training Partnership (DTP), under grant NE/S007458/1. This work was further supported by NERC, under grant

705   NE/N015657/1 (The Global Methane Budget) and NE/R001782/1 (Sources and Impacts of Short-Lived Anthropogenic Chlorine). RAL's Infrared and Microwave Sounding scheme and IASI methane scheme were developed through NERC's NCEO and MetOp-A satellite data were processed on the Jasmin computing facility managed by CEDA at RAL. We would like to thank and acknowledge Dr Katherine Travis, Dr Chris Wilson, Dr Matthew Rowlinson and Dr Ryan Hossaini for their helpful advice.

References

Anderson, D. C., Duncan, B. N., Fiore, A. M., Baublitz, C. B., Follette-Cook, M. B., Nicely, J. M. and Wolfe, G. M.: Spatial and temporal variability in the hydroxyl (OH) radical: Understanding the role of large-scale climate features and their influence on OH through its dynamical and photochemical drivers, Atmos. Chem. Phys., 21(8), 6481–6508, doi:10.5194/acp-21-6481-2021, 2021.

715   Brune, W. H., Miller, D. O., Thames, A. B., Allen, H. M., Apel, E. C., Blake, D. R., Bui, T. P., Commane, R., Crounse, J. D., Daube, B. C., Diskin, G. S., DiGangi, J. P., Elkins, J. W., Hall, S. R., Hanisco, T. F., Hannun, R. A., Hintsa, E. J., Hornbrook, R. S., Kim, M. J., McKain, K., Moore, F. L., Neuman, J. A., Nicely, J. M., Peischl, J., Ryerson, T. B., St. Clair, J. M., Sweeney, C., Teng, A. P., Thompson, C., Ullmann, K., Veres, P. R., Wennberg, P. O. and Wolfe, G. M.: Exploring Oxidation in the Remote Free Troposphere: Insights From Atmospheric Tomography

720   (ATom), J. Geophys. Res. Atmos., 125(1), 1–17, doi:10.1029/2019JD031685, 2020.

Chipperfield, M. P.: New version of the TOMCAT/SLIMCAT off-line chemical transport model: Intercomparison of stratospheric tracer experiments, Q. J. R. Meteorol. Soc., 132(617), 1179–1203, doi:10.1256/qj.05.51, 2006.

Clerbaux, C., Boynard, A., Clarisse, L., George, M., Hadji-Lazaro, J., Herbin, H., Hurtmans, D., Pommier, M., Razavi, A., Turquety, S., Wespes, C. and Coheur, P. F.: Monitoring of atmospheric composition using the thermal infrared

725   IASI/MetOp sounder, Atmos. Chem. Phys., 9(16), 6041–6054, doi:10.5194/acp-9-6041-2009, 2009.

Creasey, D. J., Evans, G. E., Heard, D. E. and Lee, J. D.: Measurements of OH and HO2 concentrations in the Southern Ocean marine boundary layer, J. Geophys. Res. Atmos., 108(15), 1–12, doi:10.1029/2002jd003206, 2003.

Dee, D. P., Uppala, S. M., Simmons, A. J., Berrisford, P., Poli, P., Kobayashi, S., Andrae, U., Balmaseda, M. A., Balsamo, G., Bauer, P., Bechtold, P., Beljaars, A. C. M., van de Berg, L., Bidlot, J., Bormann, N., Delsol, C., Dragani, R.,

730   Fuentes, M., Geer, A. J., Haimberger, L., Healy, S. B., Hersbach, H., Hólm, E. V., Isaksen, L., Kållberg, P., Köhler, M., Matricardi, M., Mcnally, A. P., Monge-Sanz, B. M., Morcrette, J. J., Park, B. K., Peubey, C., de Rosnay, P., Tavolato, C., Thépaut, J. N. and Vitart, F.: The ERA-Interim reanalysis: Configuration and performance of the data

assimilation system, Q. J. R. Meteorol. Soc., 137(656), 553–597, doi:10.1002/qj.828, 2011.

Dlugokencky, E.: NOAA Global Monitoring Laboratory - Trends in Atmospheric Methane, [online] Available from:
735   https://gml.noaa.gov/ccgg/trends_ch4/ (Accessed 1 May 2020), 2020.

Edwards, P. M., Evans, M. J., Furneaux, K. L., Hopkins, J., Ingham, T., Jones, C., Lee, J. D., Lewis, A. C., Moller, S. J.,
          Stone, D., Whalley, L. K. and Heard, D. E.: OH reactivity in a South East Asian tropical rainforest during the
          oxidant and particle photochemical processes (OP3) project, Atmos. Chem. Phys., 13(18), 9497–9514,
          doi:10.5194/acp-13-9497-2013, 2013.

740 Eisele, F. L.: Measurements and steady state calculations of OH concentrations at Mauna Loa Observatory, J. Geophys. Res.
          Atmos., 101(D9), 14665–14679, doi:10.1029/95JD03654, 1996.

European Space Agency: CCI Product Validation, [Unpublished report - available in due course]. [online] Available from:
          https://climate.esa.int/en/projects/water-vapour/key-documents/, n.d.

Faloona, I. C., Tan, D., Lesher, R. L., Hazen, N. L., Frame, C. L., Simpas, J. B., Harder, H., Martinez, M., Di Carlo, P., Ren,
745   X. and Brune, W. H.: A laser-induced fluorescence instrument for detecting tropospheric OH and HO2:
          Characteristics and calibration, J. Atmos. Chem., 47(2), 139–167, doi:10.1023/B:JOCH.0000021036.53185.0e,
          2004.

Feng, L., Smith, S. J., Braun, C., Crippa, M., Gidden, M. J., Hoesly, R., Klimont, Z., Van Marle, M., Van Den Berg, M. and
          Van Der Werf, G. R.: The generation of gridded emissions data for CMIP6, Geosci. Model Dev., 13(2), 461–482,
750   doi:10.5194/gmd-13-461-2020, 2020.

Ferracci, V., Heimann, I., Luke Abraham, N., Pyle, J. A. and Archibald, A. T.: Global modelling of the total OH reactivity:
          Investigations on the "missing" OH sink and its atmospheric implications, Atmos. Chem. Phys., 18(10), 7109–
          7129, doi:10.5194/acp-18-7109-2018, 2018.

He, J., Naik, V., Horowitz, L., Dlugokencky, E. and Thoning, K.: Investigation of the global methane budget over 1980–
755   2017 using GFDL-AM4.1, Atmos. Chem. Phys. Discuss., 20, 805–827, doi:10.5194/acp-2019-529, 2020.

Huang, J. and Prinn, R. G.: Critical evaluation of emissions of potential new gases for OH estimation, J. Geophys. Res.
          Atmos., 107(24), 1–12, doi:10.1029/2002JD002394, 2002.

Huijnen, V., Wooster, M. J., Kaiser, J. W., Gaveau, D. L. A., Flemming, J., Parrington, M., Inness, A., Murdiyarso, D.,
          Main, B. and Van Weele, M.: Fire carbon emissions over maritime southeast Asia in 2015 largest since 1997, Sci.
760   Rep., 6(May), 1–8, doi:10.1038/srep26886, 2016.

Karion, A., Sweeney, C., Wolter, S., Newberger, T., Chen, H., Andrews, A., Kofler, J., Neff, D. and Tans, P.: Long-term
          greenhouse gas measurements from aircraft, Atmos. Meas. Tech., 6(3), 511–526, doi:10.5194/amt-6-511-2013,
          2013.

Kovacs, T. A., Brune, W. H., Harder, H., Martinez, M., Simpas, J. B., Frost, G. J., Williams, E., Jobson, T., Stroud, C.,
765   Young, V., Fried, A. and Wert, B.: Direct measurements of urban OH reactivity during Nashville SOS in summer
          1999, J. Environ. Monit., 5(1), 68–74, doi:10.1039/b204339d, 2003.

Lelieveld, J., Gromov, S., Pozzer, A. and Taraborrelli, D.: Global tropospheric hydroxyl distribution, budget and reactivity, Atmos. Chem. Phys., 16(19), 12477–12493, doi:10.5194/acp-16-12477-2016, 2016.

Levy, H.: Normal atmosphere: Large radical and formaldehyde concentrations predicted, Science (80-.)., 173(3992), 141–143, doi:10.1126/science.173.3992.141, 1971.

Liang, Q., Chipperfield, M. P., Fleming, E. L., Abraham, N. L., Braesicke, P., Burkholder, J. B., Daniel, J. S., Dhomse, S., Fraser, P. J., Hardiman, S. C., Jackman, C. H., Kinnison, D. E., Krummel, P. B., Montzka, S. A., Morgenstern, O., McCulloch, A., Mühle, J., Newman, P. A., Orkin, V. L., Pitari, G., Prinn, R. G., Rigby, M., Rozanov, E., Stenke, A., Tummon, F., Velders, G. J. M., Visioni, D. and Weiss, R. F.: Deriving Global OH Abundance and Atmospheric Lifetimes for Long-Lived Gases: A Search for CH3CCl3 Alternatives, J. Geophys. Res. Atmos., 122(21), 11,914-11,933, doi:10.1002/2017JD026926, 2017.

Liu, J., Bowman, K. W., Schimel, D. S., Parazoo, N. C., Jiang, Z., Lee, M., Bloom, A. A., Wunch, D., Frankenberg, C., Sun, Y., O'Dell, C. W., Gurney, K. R., Menemenlis, D., Gierach, M., Crisp, D. and Eldering, A.: Contrasting carbon cycle responses of the tropical continents to the 2015–2016 El Niño, Science (80-.)., 358(6360), doi:10.1126/science.aam5690, 2017.

Lovelock, J. E.: Methyl chloroform in the troposphere as an indicator of OH radical abundance, Nature, 267(32), doi:https://doi.org/10.1038/267032a0, 1977.

Mann, G. W., Carslaw, K. S., Spracklen, D. V., Ridley, D. A., Manktelow, P. T., Chipperfield, M. P., Pickering, S. J. and Johnson, C. E.: Description and evaluation of GLOMAP-mode: A modal global aerosol microphysics model for the UKCA composition-climate model, Geosci. Model Dev., 3(2), 519–551, doi:10.5194/gmd-3-519-2010, 2010.

Mcnorton, J., Chipperfield, M. P., Gloor, M., Wilson, C., Feng, W., Hayman, G. D., Rigby, M., Krumme, P. B., O'Doherty, S., Prinn, R. G., Weiss, R. F., Young, D., Dlugokencky, E. and Montzka, S. A.: Role of OH variability in the stalling of the global atmospheric CH4 growth rate from 1999 to 2006, Atmos. Chem. Phys., 16(12), 7943–7956, doi:10.5194/acp-16-7943-2016, 2016.

Monks, S. A., Arnold, S. R., Hollaway, M. J., Pope, R. J., Wilson, C., Feng, W., Emmerson, K. M., Kerridge, B. J., Latter, B. L., Miles, G. M., Siddans, R. and Chipperfield, M. P.: The TOMCAT global chemical transport model v1.6: Description of chemical mechanism and model evaluation, Geosci. Model Dev., doi:10.5194/gmd-10-3025-2017, 2017.

Montzka, S. A., Krol, M., Dlugokencky, E., Hall, B. and Jo, P.: Small Interannual Variability of Global Atmospheric Hydroxyl, Science (80-.)., 331(January), 67–69, 2011.

Morgenstern, O., Hegglin, M., Rozanov, E., O'Connor, F., Luke Abraham, N., Akiyoshi, H., Archibald, A., Bekki, S., Butchart, N., Chipperfield, M., Deushi, M., Dhomse, S., Garcia, R., Hardiman, S., Horowitz, L., Jöckel, P., Josse, B., Kinnison, D., Lin, M., Mancini, E., Manyin, M., Marchand, M., Marécal, V., Michou, M., Oman, L., Pitari, G., Plummer, D., Revell, L., Saint-Martin, D., Schofield, R., Stenke, A., Stone, K., Sudo, K., Tanaka, T., Tilmes, S., Yamashita, Y., Yoshida, K. and Zeng, G.: Review of the global models used within phase 1 of the Chemistry-

Climate Model Initiative (CCMI), Geosci. Model Dev., 10(2), 639–671, doi:10.5194/gmd-10-639-2017, 2017.

Naik, V., Voulgarakis, A., Fiore, A. M., Horowitz, L. W., Lamarque, J. F., Lin, M., Prather, M. J., Young, P. J., Bergmann, D., Cameron-Smith, P. J., Cionni, I., Collins, W. J., Dalsøren, S. B., Doherty, R., Eyring, V., Faluvegi, G., Folberth, G. A., Josse, B., Lee, Y. H., MacKenzie, I. A., Nagashima, T., Van Noije, T. P. C., Plummer, D. A., Righi, M., Rumbold, S. T., Skeie, R., Shindell, D. T., Stevenson, D. S., Strode, S., Sudo, K., Szopa, S. and Zeng, G.: Preindustrial to present-day changes in tropospheric hydroxyl radical and methane lifetime from the Atmospheric Chemistry and Climate Model Intercomparison Project (ACCMIP), Atmos. Chem. Phys., 13(10), 5277–5298, doi:10.5194/acp-13-5277-2013, 2013.

Naus, S., Montzka, S. A., Pandey, S., Basu, S., Dlugokencky, E. J. and Krol, M.: Constraints and biases in a tropospheric two-box model of OH, Atmos. Chem. Phys., 19(1), 407–424, doi:10.5194/acp-19-407-2019, 2019.

NOAA: Multivariate ENSO Index Version 2 (MEI.v2), [online] Available from: https://psl.noaa.gov/enso/mei/ (Accessed 11 September 2021), 2021.

Nölscher, A. C., Yañez-Serrano, A. M., Wolff, S., De Araujo, A. C., Lavrič, J. V., Kesselmeier, J. and Williams, J.: Unexpected seasonality in quantity and composition of Amazon rainforest air reactivity, Nat. Commun., 7, doi:10.1038/ncomms10383, 2016.

Patra, P. K., Krol, M. C., Prinn, R. G., Takigawa, M., Mühle, J., Montzka, S. A., Lal, S., Yamashita, Y., Naus, S., Chandra, N., Weiss, R. F., Krummel, P. B., Fraser, P. J., O'Doherty, S. and Elkins, J. W.: Methyl Chloroform Continues to Constrain the Hydroxyl (OH) Variability in the Troposphere, J. Geophys. Res. Atmos., 126(4), doi:10.1029/2020JD033862, 2021.

Podolske, J. R., Sachse, G. W. and Diskin, G. S.: Calibration and data retrieval algorithms for the NASA Langley/Ames Diode Laser Hygrometer for the NASA Transport and Chemical Evolution over the Pacific (TRACE-P) mission, J. Geophys. Res. Atmos., 108(20), 1–9, doi:10.1029/2002jd003156, 2003.

Pope, R. J., Kerridge, B. J., Siddans, R., Latter, B. G., Chipperfield, M. P., Arnold, S. R., Ventress, L. J., Pimlott, M. A., Graham, A. M., Knappett, D. S. and Rigby, R.: Large enhancements in southern hemisphere satellite-observed trace gases due to the 2019/2020 Australian wildfires, J. Geophys. Res. Atmos., 1–13, doi:10.1029/2021jd034892, 2021.

Prinn, R., Cunnold, D., Simmonds, P., Alyea, F., Boldi, R., Crawford, A., Fraser, P., Gutzler, D., Hartley, D., Rosen, R. and Rasmussen, R.: Global average concentration and trend for hydroxyl radicals deduced from ALE/GAGE trichloroethane (methyl chloroform) data for 1978–1990, J. Geophys. Res., 97(D2), 2445, doi:10.1029/91jd02755, 1992.

Prinn, R. G., Huang, J., Weiss, R. F., Cunnold, D. M., Fraser, P. J., Simmonds, P. G., McCulloch, A., Harth, C., Salameh, P., O'Doherty, S., Wang, R. H. J., Porter, L. and Miller, B. R.: Evidence for substantial variations of atmospheric hydroxyl radicals in the past two decades, Science (80-.)., 292(5523), 1882–1888, doi:10.1126/science.1058673, 2001.

Prinn, R. G., Huang, J., Weiss, R. F., Cunnold, D. M., Fraser, P. J., Simmonds, P. G., McCulloch, A., Harth, C., Reimann, S.,

835   Salameh, P., O'Doherty, S., Wang, R. H. J., Porter, L. W., Miller, B. R. and Krummel, P. B.: Evidence for variability of atmospheric hydroxyl radicals over the past quarter century, Geophys. Res. Lett., 32(7), 1–4, doi:10.1029/2004GL022228, 2005.

Rigby, M., Montzka, S. A., Prinn, R. G., White, J. W. C., Young, D., O'Doherty, S., Lunt, M. F., Ganesan, A. L., Manning, A. J., Simmonds, P. G., Salameh, P. K., Harth, C. M., Mühle, J., Weiss, R. F., Fraser, P. J., Steele, L. P., Krummel,
840   P. B., McCulloch, A. and Park, S.: Role of atmospheric oxidation in recent methane growth, Proc. Natl. Acad. Sci. U. S. A., 114(21), 5373–5377, doi:10.1073/pnas.1616426114, 2017.

Rowlinson, M. J., Rap, A., Arnold, S. R., Pope, R. J., Chipperfield, M. P., McNorton, J., Forster, P., Gordon, H., Pringle, K. J., Feng, W., Kerridge, B. J., Latter, B. L. and Siddans, R.: Impact of El Niño Southern Oscillation on the interannual variability of methane and tropospheric ozone, Atmos. Chem. Phys. Discuss., 2, 1–20, doi:10.5194/acp-
845   2019-222, 2019.

Ryerson, T. B., Williams, E. J. and Fehsenfeld, F. C.: An efficient photolysis system for fast-response NO2 measurements, J. Geophys. Res. Atmos., 105(D21), 26447–26461, doi:10.1029/2000JD900389, 2000.

Savage, N. H., Harrison, R. M., Monks, P. S. and Salisbury, G.: Steady-state modelling of hydroxyl radical concentrations at Mace Head during the EASE '97 campaign, May 1997, Atmos. Environ., doi:10.1016/S1352-2310(00)00315-0,
850   2001.

Shetter, R. E. and Müller, M.: Photolysis frequency measurements using actinic flux spectroradiometry during the PEM-Tropics mission: Instrumentation description and some results, J. Geophys. Res. Atmos., 104(D5), 5647–5661, doi:10.1029/98JD01381, 1999.

Siddans, R., Knappett, D., Kerridge, B., Waterfall, A., Hurley, J., Latter, B., Boesch, H. and Parker, R.: Global height-
855   resolved methane retrievals from the Infrared Atmospheric Sounding Interferometer (IASI) on MetOp, Atmos. Meas. Tech., 10(11), 4135–4164, doi:10.5194/amt-10-4135-2017, 2017.

Siddans, R., Knappett, D., Kerridge, B., Latter, B. and Waterfall, A.: STFC RAL methane retrievals from IASI on board MetOp-A, version 2.0, , doi:10.5285/f717a8ea622f495397f4e76f777349d1, 2020.

Singh, H. B.: Preliminary estimation of average tropospheric HO concentrations in the northern and southern hemispheres,
860   Geophys. Res. Lett., doi:10.1029/GL004i010p00453, 1977.

Slater, E. J., Whalley, L. K., Woodward-Massey, R., Ye, C., Lee, J. D., Squires, F., Hopkins, J. R., Dunmore, R. E., Shaw, M., Hamilton, J. F., Lewis, A. R., Crilley, L. R., Kramer, L., Bloss, W., Vu, T., Sun, Y., Xu, W., Yue, S., Ren, L., Joe, W., Nicholas Hewitt, C., Wang, X., Fu, P. and Heard, D. E.: Elevated levels of OH observed in haze events during wintertime in central Beijing, Atmos. Chem. Phys., 20(23), 14847–14871, doi:10.5194/acp-20-14847-2020,
865   2020.

Smith, S. C., Lee, J. D., Bloss, W. J., Johnson, G. P., Ingham, T. and Heard, D. E.: Concentrations of OH and HO2 radicals during NAMBLEX: Measurements and steady state analysis, Atmos. Chem. Phys., 6(5), 1435–1453, doi:10.5194/acp-6-1435-2006, 2006.

Sommariva, R., Haggerstone, A.-L., Carpenter, L. J., Carslaw, N., Creasey, D. J., Heard, D. E., Lee, J. D., Lewis, A. C., Pilling, M. J. and Zádor, J.: OH and HO2 chemistry in clean marine air during SOAPEX-2, Atmos. Chem. Phys., 4(3), 839–856, doi:10.5194/acp-4-839-2004, 2004.

Spivakovsky, C. M., Logan, J. A., Montzka, S. A., Balkanski, Y. J., Foreman-Fowler, M., Jones, D. B. A., Horowitz, L. W., Fusco, A. C., Brenninkmeijer, C. A. M., Prather, M. J., Wofsy, S. C. and McElroy, M. B.: Three-dimensional climatological distribution of tropospheric OH: Update and evaluation, J. Geophys. Res. Atmos., 105(D7), 8931–8980, doi:10.1029/1999JD901006, 2000.

Stone, D., Whalley, L. K. and Heard, D. E.: Tropospheric OH and HO2 radicals: Field measurements and model comparisons, Chem. Soc. Rev., 41(19), 6348–6404, doi:10.1039/c2cs35140d, 2012.

Streets, D. G., Canty, T., Carmichael, G. R., De Foy, B., Dickerson, R. R., Duncan, B. N., Edwards, D. P., Haynes, J. A., Henze, D. K., Houyoux, M. R., Jacob, D. J., Krotkov, N. A., Lamsal, L. N., Liu, Y., Lu, Z., Martin, R. V., Pfister, G. G., Pinder, R. W., Salawitch, R. J. and Wecht, K. J.: Emissions estimation from satellite retrievals: A review of current capability, Atmos. Environ., 77(2013), 1011–1042, doi:10.1016/j.atmosenv.2013.05.051, 2013.

Thames, A. B., Brune, W. H., Miller, D. O., Allen, H. M., Apel, E. C., Blake, D. R., Paul Bui, T., Commane, R., Crounse, J. D., Daube, B. C., Diskin, G. S., Digangi, J. P., Elkins, J. W., Hall, S. R., Hanisco, T. F., Hannun, R. A., Hintsa, E., Hornbrook, R. S., Kim, M. J., McKain, K., Moore, F. L., Nicely, J. M., Peischl, J., Ryerson, T. B., St. Clair, J. M., Sweeney, C., Teng, A., Thompson, C. R., Ullmann, K., Wennberg, P. O. and Wolfe, G. M.: Missing OH reactivity in the global marine boundary layer, Atmos. Chem. Phys., 20(6), 4013–4029, doi:10.5194/acp-20-4013-2020, 2020.

Travis, K., Heald, C., Allen, H., Apel, E., Arnold, S., Blake, D., Brune, W., Chen, X., Commane, R., Crounse, J., Daube, B., Diskin, G., Elkins, J., Evans, M., Hall, S., Hintsa, E., Hornbrook, R., Kasibhatla, P., Kim, M., Luo, G., McKain, K., Millet, D., Moore, F., Peischl, J., Ryerson, T., Sherwen, T., Thames, A., Ullmann, K., Wang, X., Wennberg, P., Wolfe, G. and Yu, F.: Constraining remote oxidation capacity with ATom observations, Atmos. Chem. Phys. Discuss., (January), 1–41, doi:10.5194/acp-2019-931, 2020.

Turner, A. J., Frankenberg, C., Wennberg, P. O. and Jacob, D. J.: Ambiguity in the causes for decadal trends in atmospheric methane and hydroxyl, Proc. Natl. Acad. Sci. U. S. A., 114(21), 5367–5372, doi:10.1073/pnas.1616020114, 2017.

Turner, A. J., Frankenberg, C. and Kort, E. A.: Interpreting contemporary trends in atmospheric methane, Proc. Natl. Acad. Sci. U. S. A., 116(8), 2805–2813, doi:10.1073/pnas.1814297116, 2019.

Voulgarakis, A., Marlier, M. E., Faluvegi, G., Shindell, D. T., Tsigaridis, K. and Mangeon, S.: Interannual variability of tropospheric trace gases and aerosols: The role of biomass burning emissions, J. Geophys. Res. Atmos., 120, 7157–7173, doi:http://dx.doi.org/10.1002/2014JD022926, 2015.

van der Werf, G. R., Randerson, J. T., Giglio, L., Van Leeuwen, T. T., Chen, Y., Rogers, B. M., Mu, M., Van Marle, M. J. E., Morton, D. C., Collatz, G. J., Yokelson, R. J. and Kasibhatla, P. S.: Global fire emissions estimates during 1997-2016, Earth Syst. Sci. Data, 9(2), 697–720, doi:10.5194/essd-9-697-2017, 2017.

Wofsy, S. C., Afshar, S., Allen, H. M., Apel, E., Asher, E. C., Bar letta, B., Bent, J., Bian, H., Biggs, B. C., Blake, D. R.,

Blake, N., Bourgeois, I., Brock, C. A., Brune, W. H., Budney, J. W., Bui, T. P., Butler, A., Campuzano-Jost, P., Chang, C. S., Chin, M., Commane, R., Correa, G., Crounse, J. D., Cullis, P. D., Daube, B. C., Day, D. A., Dean-Day, J. M., Dibb, J. E., Di Gangi, J. P., Diskin, G. S., Dollner, M., Elkins, J. W., Erdesz, F., Fiore, A. M., Flynn, C. M., Froyd, K., Gesler, D. W., Hall, S. R., Hanisco, T. F., Hannun, R. A., Hills, A. J., Hintsa, E. J., Hoffman, A., Hornbrook, R. S., Huey, L. G., Hughes, S., Jimenez, J. L., Johnson, B. J., Katich, J. M., Keeling, R. F., Kim, M. J., Kupc, A., Lait, L. R., Lamarque, J.-F., Liu, J., McKain, K., Mclaughlin, R. J., Meinardi, S., Miller, D. O., Montzka, S. A., Moore, F. L., Morgan, E. J., Murphy, D. M., Murray, L. T., Nault, B. A., Neuman, J. A., Newman, P. A., Nicely, J. M., Pan, X., Paplawsky, W., Peischl, J., Prather, M. J., Price, D. J., Ray, E., Reeves, J. M., Richardson, M., Rollins, A. W., Rosenlof, K. H., Ryerson, T. B., Scheuer, E., Schill, G. P., Schroder, J. C., Schwarz, J. P., St. Clair, J. M., Steenrod, S. D., Stephens, B. B., Strode, S. A., Sweeney, C., Tanner, D., Teng, A. P., Thames, A. B., Thompson, C. R., Ullmann, K., Veres, P. R., Vieznor, N., Wagner, N. L., Watt, A., Weber, R., Weinzierl, B., et al.: ATom: Merged Atmospheric Chemistry, Trace Gases, and Aerosols, ORNL Distrib. Act. Arch. Cent., doi:10.3334/ORNLDAAC/1581, 2018.

Wolfe, G. M., Nicely, J. M., Clair, J. M. S., Hanisco, T. F., Liao, J., Oman, L. D., Brune, W. B., Miller, D., Thames, A., Abad, G. G., Ryerson, T. B., Thompson, C. R., Peischl, J., McKain, K., Sweeney, C., Wennberg, P. O., Kim, M., Crounse, J. D., Hall, S. R., Ullmann, K., Diskin, G., Bui, P., Chang, C. and Dean-Day, J.: Mapping hydroxyl variability throughout the global remote troposphere via synthesis of airborne and satellite formaldehyde observations (Proceedings of the National Academy of Sciences of the United States of America (2019) 116 (11171–11180) DOI: 10.1073/, Proc. Natl. Acad. Sci. U. S. A., 116(26), 13144, doi:10.1073/pnas.1908931116, 2019.

Yang, Y., Shao, M., Wang, X., Nölscher, A. C., Kessel, S., Guenther, A. and Williams, J.: Towards a quantitative understanding of total OH reactivity: A review, Atmos. Environ., 134(2), 147–161, doi:10.1016/j.atmosenv.2016.03.010, 2016.

Zhao, Y., Saunois, M., Bousquet, P., Lin, X., Berchet, A., Hegglin, M., Canadell, J., Jackson, R., Deushi, M., Jöckel, P., Kinnison, D., Kirner, O., Strode, S., Tilmes, S., Dlugokencky, E. and Zheng, B.: On the role of trend and variability of hydroxyl radical (OH) in the global methane budget, Atmos. Chem. Phys. Discuss., 2011, 1–28, doi:10.5194/acp-2020-308, 2020.